



Aerodynamic Wind Tunnel in Passenger Car Application

by

ZHIPENG LYU

A Thesis Submitted in
Partial fulfilment of the
Requirements for the Degree of

Master of Science

Thesis supervisors:

Stefan Wallin-PhD.
Dept. of Mechanics, KTH

Pirooz Moradnia –PhD.
Env. & Fluid Dyn. Centre, Volvo Car Corporation



Acknowledgement

I would like to express my gratitude to my supervisor Dr. Pirooz Moradnia at Volvo Car Corporation for his continuous guidance, endless support and engagement through the learning process of this master thesis. Furthermore I would like to thank Dr. Stefan Wallin at Dept. of Mechanics, KTH for all the support and advice during the entire process. Also, I would like to thank my colleagues at Volvo, who have willingly shared their precious time during the entire process. I would also like to thank Volvo Car Cooperation for the opportunity to learn and practice.

Finally, I must express my very profound gratitude to my parents for providing me with unfailing support and continuous encouragement throughout my years of study and through the process of researching and writing this thesis. This accomplishment would not have been possible without them.

Zhipeng Lyu

Contents

Abstract	5
Introduction	6
1. Measurement and simulation equipment	6
1.1. Force measurement	6
1.2. Pressure measurements	10
1.3. Boundary layer control system(BLC)	10
1.4. Cooling system	11
1.5. Rotating wheel system	12
2. Flow Quality	12
2.1. Airspeed calibrations	12
2.2. Boundary layer control system (BLC) study	14
2.2.1. Induced effects on flow quality by BLC	14
2.2.2. Boundary layer measurements	14
2.3. Horizontal buoyancy	22
3. Measurement quality	24
3.1. Reynolds Sweep Repeatability	24
3.2. Yaw sweep repeatability	25
4. Correlation force measurement	27
4.1. Experimental setup	27
4.2. Trend prediction	28
4.3. Differential force prediction	31
5. Correlation unsteady base pressure measurement	32
5.1. Experimental Setup	33
5.2. Results for full scale tests	34
5.2.1. Wake pumping mode	34
5.2.2. Vortex shedding modes	36
5.2.3. Wake center	37
5.3. Comparison of PVT and MWT Results	38
5.4. Coherence analysis	40
6. Conclusion	42
References	43
Appendix	44

List of Figures

i	Layout of the Volvo full-scale wind tunnel (PVT)	6
1.1	Force balance struts	7
1.2	Linkage system	7
1.3	Variation of drag coefficient of blunt and streamlined bodies with Reynolds number	8
1.4	Balance calibration quality	9
1.5	Boundary layer control system layout	11
2.1	Measurement locations of differential pressure	12
2.2	Airspeed calibration setup	13
2.3	Airspeed calibration results	13
2.4	Airspeed stability with respect to fan capacity	14
2.5	Rake installation	15
2.6	Rake traversing	15
2.7	Boundary layer profile in the center of the turntable at test airspeed 30m/s	16
2.8	Boundary layer profile logarithmic regression in linear scale	17
2.9	Boundary layer profile logarithmic regression in semi-log scale	17
2.10	Traversing gear measurement Area	18
2.11	Boundary Layer profile with BLC at 50m/s	18
2.12	Boundary Layer profile without BLC at 50m/s	19
2.13	Turbulent boundary layer classification	19
2.14	Velocity profiles for prediction model and measurement	21
2.15	Velocity profiles for prediction model and measurement near the wall(semi-log)	21
2.16	Flow acceleration due to boundary layer development	22
2.17	Static pressure measurements along the test section	22
2.18	Static pressure distribution along the test section	23
3.1	Square back	24
3.2	Fastback	24
3.3	Airspeed dependence on repeatability for square back.	24
3.4	Airspeed dependence on repeatability for fastback	25
3.5	Yaw dependence on repeatability for square back	26
3.6	Yaw dependence on repeatability for fastback	26
4.1	Full scale Aero 2020	27
4.2	1/5 th scale Aero 2020	27
4.3	Rear roof wing extension	28
4.4	Front wheel bay ribs	28
4.5	Front wheel cover	28
4.6	Reynolds number extrapolation effect	29
4.7	Comparison of differential front axle lift coefficients for scaled and full scale tests	30
4.8	Comparison of differential rear axle lift coefficients for scaled and full scale tests	30
4.9	Differential Cd Comparison of Full scale and 1/5 th Car	31
4.10	Differential Clf Comparison of Full Scale and 1/5 th Car	31
4.11	Differential Clr Comparison of Full Scale and 1/5 th Scale Car	32
5.1	Critical frequency range for full-scale vehicle dynamics	32

5.2	Pressure sensors on full scale car	33
5.3	Pressure sensors on model car	33
5.4	Sensors locations on full scale car	34
5.5	Sensors locations on model car	34
5.6	Free stagnation point fluctuation in longitudinal direction	35
5.7	POD Mode 4-wake pumping	35
5.8	POD Mode 1-wake flapping	36
5.9	POD Mode 2-trapped Vortex	36
5.10	Regions of interest for wake center determination	37
5.11	Lateral distributions of wake centers at three regions	37
5.12	Vertical distributions of wake centers at three regions	38
5.13	Pressure power spectral densities comparison between PVT and MWT	39
5.14	Coherence of opposite positions on the model base	41
A1	Static pressure distribution along the test section	44
A2	Flow recirculation through sudden expansion	44
A3	Measurement area	45
A4	Total pressure distribution behind the BLC system	46
A5	Airspeed dependence on moments' repeatability of square back	46
A6	Airspeed dependence on moments' repeatability of fastback	47
A7	Yaw dependence on moments' repeatability of square back	47
A8	Yaw dependence on moments' repeatability of fastback	47
A9	POD Mode 3	48

List of Tables

1	Balance system calibration targets	9
2	Confidence intervals-force measurement	10
3	Boundary layer characteristics at test airspeed 30m/s with BLC on	16
4	Characteristic roughness for different types of turbulent BL	20
5	Shear velocities for prediction model and measurement	21
6	Maximum resultant drag due to horizontal buoyancy	23
7	Maximum Deviances in measurements at airspeed of 50m/s	25
8	Maximum Deviances in measurements at 15° and 5° yaw	27
9	Details of Full Scale and 1/5th Scale Clay Car	27

Abstract

The thesis aims to provide an evaluation on the Volvo 1/5th scaled wind tunnel regarding its potentials and capabilities in aerodynamic study. The flow quality in the test section was evaluated. The experiments were performed included measurements of airspeed stability, tunnel-wall boundary layer profile and horizontal buoyancy. A numerical model was developed to predict the boundary layer thickness on the test floor. Repeatability tests were also conducted to establish the appropriate operating regime.

A correlation study between the 1/5th scaled wind tunnel (MWT) and full scale wind tunnel (PVT) was performed using steady force and unsteady pressure measurements. The Volvo Aero 2020 concept car was selected to be the test model.

The Reynolds effect and the tunnel-wall boundary layer interference were identified in the steady force measurements. Unsteady near-wake phenomena such as wake pumping and wake flapping were discussed in the unsteady base pressure measurements.

Keywords: Vehicle aerodynamics, 1/5th scale wind tunnel, unsteady pressure measurements, wind tunnel effects

Introduction

The use of low-speed wind tunnels in the field of ground transportation has been very active over the past decade. During this period the wind tunnel has been used more frequently in solving vehicle aerodynamic problems due to its large impact on fuel efficiency, driving characteristics, etc. However, the cost of wind tunnel operation on a full scale vehicle is fairly high. One alternative is to perform the tests in a scaled wind tunnel.

The model wind tunnel, built in 1984 is a 1:5 scale wind tunnel. It is built as a prototype for the full scale wind tunnel (PVT) to study the feasibility of the slotted-wall test section. The full scale tunnel's closed air-path can be seen in Figure i. The test facility featured a horizontally closed air-path with a 1.1 m^2 test section of slotted walls and ceiling, where the longitudinal slots created a 30% open-area ratio to minimize the blockage effects of the solid walls. The maximum air speed is 54m/s in the test section. The test section is equipped with a boundary layer control system, external 6-balance scale system and traversing gear.

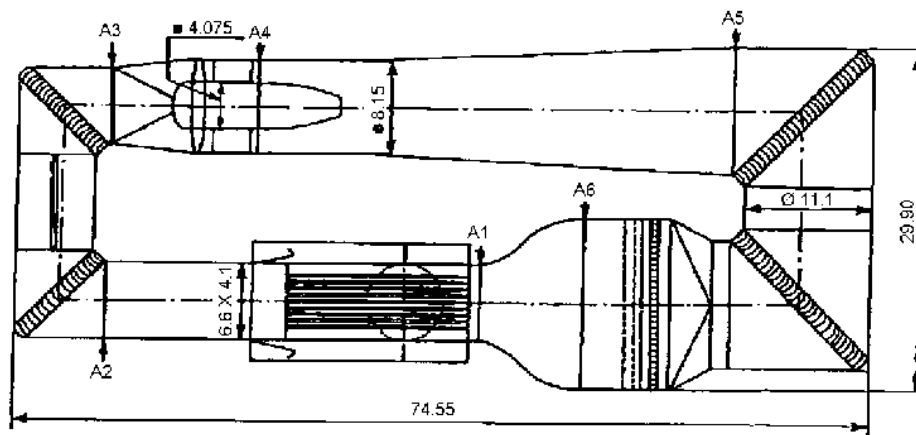


Figure i: Layout of the Volvo full-scale wind tunnel (PVT)

1. Measurement and simulation equipment

1.1. Force measurement

The aerodynamic loads on the test model are measured by a 6-component balance located underneath the test floor. The test model is mounted on 4 balance struts with circular cross sections, the positions of which can be adjusted according to the test model geometry, as shown in figure 1.1. The struts separate the aerodynamic forces and moments using a linkage system as shown in figure 1.2 and feed the loads to measuring units. The analog signal transmitted by the strain gauges is scaled by an amplifier and then transformed into digital form by an A/D transducer. The *labView* program is used to process the signal.

A body axis system is used for measurements, forces and moments are measured parallel and perpendicular to the longitudinal axis of the test model, thus the coordinates system yaws with the model, the roll and pitch angles are generally set to zero and remain constant once the model is mounted on the balance struts. The non-dimensional aerodynamic coefficients are then calculated given the characteristic dimension of the test model and the dynamic pressure.

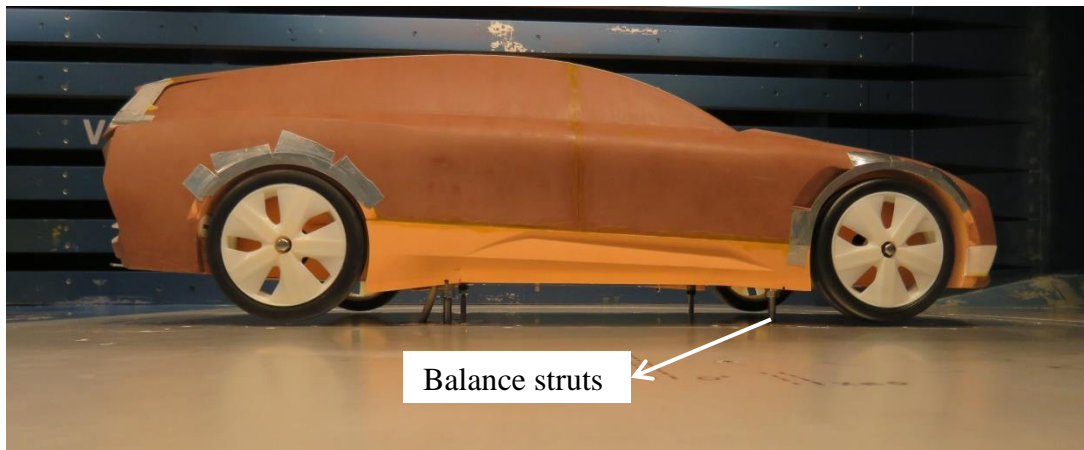


Figure 1.1: Force balance struts

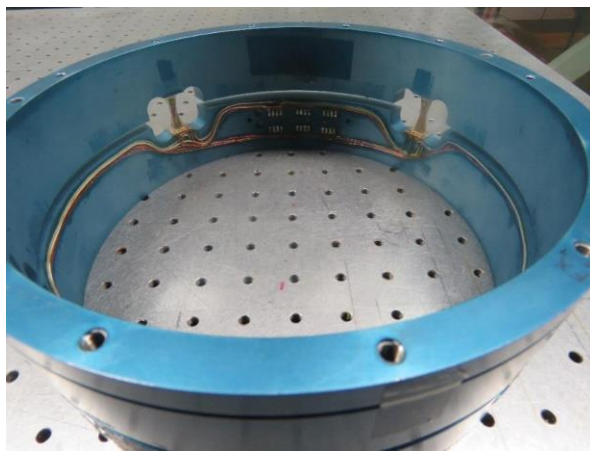


Figure 1.2: Linkage system

Additional aerodynamic loads will emerge for every strut connecting the model to the balance system. The most obvious quantity in the force measurements influenced by the exposed struts is drag. However, due to the complex aerodynamic interaction of the struts with the car underbody and wheels, a simple load measurement of aero-forces on the struts in an empty wind tunnel is not sufficient to evaluate this effect. The minimum drag criterion should be employed when designing the model chassis such that the balance struts are shielded by the front wheels. Since the aerodynamic loads are proportional to the kinetic energy in the streamwise direction, the turbulent wheel wake flow with lower streamwise kinetic energy will reduce the resultant drag on the struts and the interference with the airfield at small yaw angles, but full exposure to the mainstream is still possible for large yaw angle tests. The maximum Reynolds number for a full exposed strut with a diameter of 7mm is around 2×10^4 , which is far below the critical Reynolds number for a circular cylinder, namely from 10^5 to 10^6 as shown in figure 1.3. The drag coefficient variation on the balance struts due to the Reynolds effect is therefore controlled.

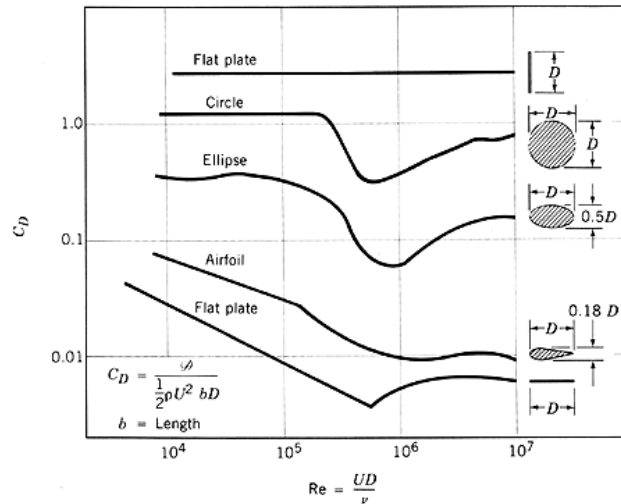


Figure 1.3: Variation of drag coefficient of blunt and streamlined bodies with Reynolds number {1}

Another negative impact on the test section flow from the ordinary balance system originates from air leakage. Openings are designed on the bottom of the balance shield chamber to allow for the signal cable to pass through. The static pressure in the test section is generally below the atmospheric pressure, the resulting differential pressure tends to draw the air from the surroundings into the test section through the balance chamber. Thus air sealing should be applied to close off the balance chamber. An offset calibration is required before any measurement to level out the strains on the balance struts once the test model is mounted. The calibration quality is checked by measuring the forces and moments at zero airspeed. The targets of the calibration results are specified below in table 1{2}. To minimize the measurement uncertainties introduced by the balance system, the calibration targets must be met until one can proceed to the measurements.

Table 1: Balance system calibration targets

FX(Drag Force)	FY(Side Force)	FZ(Lift Force)
±0.036N	±0.027N	±0.080N

The calibration should be performed with still air in the test section as well as in the test room; minimum background disturbances are also required with the cooling, the boundary layer control and the rotating wheel systems off. The calibration quality suffers mostly from two effects:

- Air recirculation in the test section due to air leakage around the main entrance gate degrades the calibration quality. The air recirculation is mainly fed by the temperature gradient between the test section and the test room. The calibrations are valid only if the targets are met with measured Reynolds number equal to zero.
- Mechanical vibrations from surrounding environment would introduce changes in strain that detectable by the sensors. This effect could be greater than the first one but can be easily eliminated by repeating the calibration.

10 trails of zero speed measurements were performed after the calibration targets are met and the results for all forces are shown in figure 1.4. Each data point represents the average value of 600 measurements and the calibration targets are highlighted in solid lines.

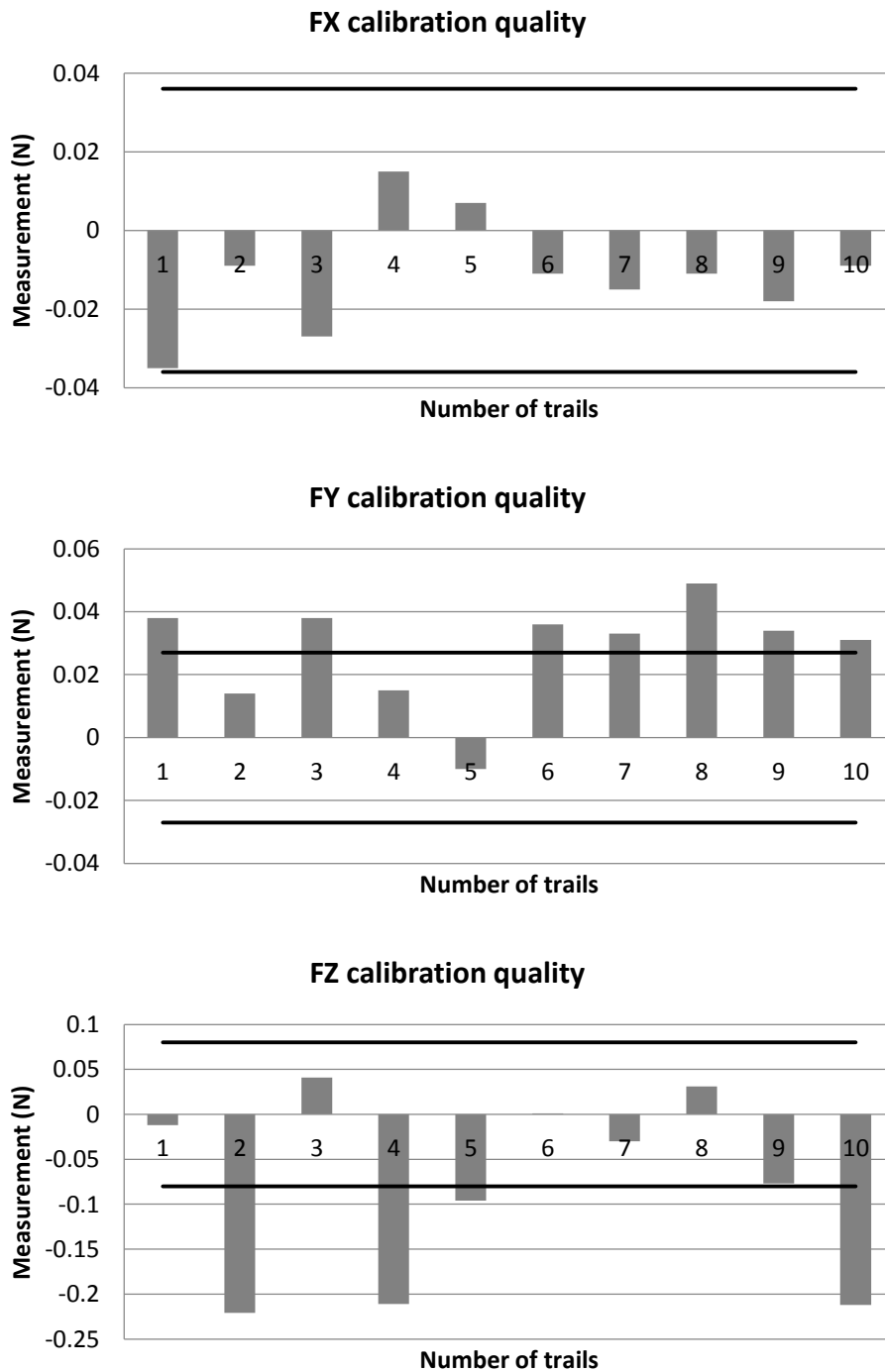


Figure 1.4: Balance calibration quality

The side and lift forces measurements were found to be more sensitive to background disturbances. The effect of disturbances during the test can be minimized by taking an arithmetic average over a larger number of samples, 3000-4000 samples are recommended to ensure the accuracy.

The accuracy of the force measurements is evaluated by the confidence interval, which defines the range of values on either side of a given single measurement in which 95% certainty can be achieved that the true mean value lies {3}. It is given by:

$$e_x = t_{95\%}\sigma_s$$

Where σ_s is the standard deviation calculated over the measurement population and $t_{95\%} = 1.645$ is obtained from t-distribution table for a large sample size of 3000 ensembles. The confidence interval for the force measurement is given in table 2:

Table 2: Confidence intervals-force measurement

FX(Drag Force)	FY(Side Force)	FZ(Lift Force)
$\pm 0,302\text{N}$	$\pm 0,348\text{N}$	$\pm 0,894\text{N}$

Note that the confidence intervals reveal the overall uncertainties presented in force measurement, it involves the accuracy of the balance system, airspeed stability, background noise, etc.

1.2. Pressure measurements

The pressure acquisition is performed by the *PSI 8400* system with guaranteed accuracy of $\pm 2.5\text{pa}$ for up to 4096 channels. ESP pressure scanners with 16, 32 or 64 ports per scanner are integrated with A/D transmission to the host system. The system is capable of performing unsteady pressure measurement when equipped with fast response pressure sensors.

With the traversing gear downstream of the turntable, a wake measurement can be performed. The traversing gear is composed of two sets of step motor servo systems that enable the probe holder to move in lateral and vertical directions. The customized probe holder is capable of holding five 7-hole pressure probes in total. A detailed wake measurement regarding velocity amplitude and angularity is possible after the pressure probes are calibrated. A Special rig is required for such calibrations which are usually conducted by the probe manufacturer.

The calibration of the pressure measurement system is mainly done on the ESP pressure scanner. Channels that will be used for measurements are calibrated against 5 known pressures. The pressure pack usually contains values above, below and equal to the atmospheric pressure and the measurement range is bounded by the maximum and minimum values in the pack. The Pressurized air and the vacuum pump should be connected to the system during the calibration as pressure sources. The system uses a piston valve system to achieve accurate pressure output for the calibration pack. A forth order polynomial calibration function is calculated automatically by the system after measuring the responses from each channel. The calibration coefficients can be saved and exported, but a three-month cycle is recommended for pressure system calibration.

1.3. Boundary layer control system(BLC)

The level floor in the test section is used as the road in automotive wind tunnels. However the presence of the boundary layer on the level floor introduces major differences in the flow field when comparing to that of real driving condition so that the measured lift and drag are in error. To improve the simulation of road in wind tunnel tests, a boundary layer control system that creates a distributed suction area in front of the test model is used. By removing a portion of the flow with lower kinetic energy compared to that of the free stream, the boundary layer thickness is reduced significantly. The mass flow removed by the distributed suction will be recirculated back into the test section from outside the slotted walls, as shown in figure 1.5.

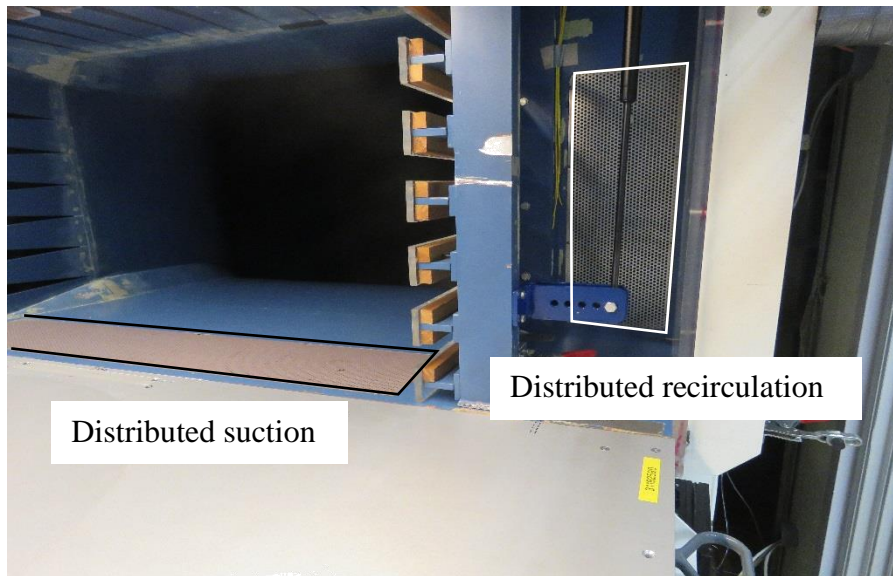


Figure 1.5: Boundary layer control system layout

The mass flow removed by the BLC can be adjusted by controlling the angular velocity of the suction fan. The current setting for BLC in terms of angular frequency is 34.7Hz, which is optimized at airspeed of 53m/s according to the user manual. The corresponding boundary layer thickness at the middle of the turntable is 15mm when the BLC is activated.

1.4. Cooling system

The energy supplied to the fan eventually dissipates into heat as the flow travels through the tunnel. Temperature grows continually until the thermal equilibrium between the dissipation and heat transfer is established. The equilibrium is realized at reasonable temperatures for low-speed open jets tunnels. For wind tunnels with closed test section, however, the equilibrium is often established at rather high temperatures. The high temperature test condition is not favorable for the model wind tunnel tests as:

- For geometrical modifications sculptured by clay and/or wax, high-temperature test conditions could soften the material rapidly, thus lead to geometrical deformation and even damage under high dynamic pressures.
- The Reynolds number drops at high temperature since the air viscosity increases with respect to temperature. The model wind tunnel tests will further deviate from the real driving condition as a result of high temperature.

The air flow temperature is stabilized by an inbuilt heat radiator using water as cooling medium. An internal heat exchanger is installed in the largest tunnel section where the stream temperature is highest and the dynamic pressure is lowest, so that the pressure drop across the heat radiator would be minimized [4]. Since no active temperature control is available, the temperature of the air flow cannot be set at a fixed value for different test conditions, as it could be affected by time of operation, room temperature and airspeeds. However in practice the variation in temperature is not taken into account since the variation range is usually within 2°C and the corresponding change in Reynolds number is negligible. Each measurement should be taken after thermal equilibrium is established, normally it takes 3-5 minutes for the temperature to settle down and remain relatively constant.

The temperature will be registered automatically by the *labView* program for air density calculation using the ideal gas law:

$$P = \rho RT$$

The atmospheric pressure should be read manually from the aneroid barometer and its value will be used as an input in *labView*. The air density will be used for airspeed calculation and will be discussed in the *Airspeed calibrations*.

1.5. Rotating wheel system

To improve the simulations of on-road driving conditions, a rotating wheel system is installed on the chassis of the test model. It is composed of two DC motor servo circuits with a velocity regulated control protocol. The angular velocity of the wheels during the tests is set to match the airspeed based on the radius of the wheels. Mechanical vibrations are however inevitable due to uneven mass distribution between wheels and suspension systems on the driver and passenger side. Vibrations are notable at low wheel angular velocities and decay as the angular velocity increases, thus a minimum of 1.5mm ground clearance is required between the wheels and the test floor to allow the free rotation.

2. Flow Quality

2.1. Airspeed calibrations

Since the airspeed is not perfectly uniform throughout the test section, the reference test airspeed is evaluated in the middle of the test section above the turntable {2}. In practice, however, the test airspeed is not measured inside the test section using a Pitot-Static probe since the presence of the probe will influence the air field around the test model.

The test airspeed is determined by measuring the differential static pressure between two pressure ports Pc1 and Pc2, which are located at the start and the end of the contraction section correspondingly, as shown in figure 2.1. The pressure difference is read by a differential pressure transducer and the signal is registered in *labView*.

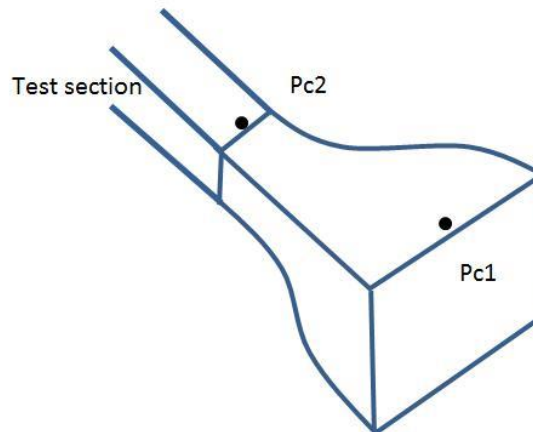


Figure 2.1: Measurement locations of differential pressure

The airspeed at the test section can be calculated theoretically for a perfect compressible gas based on isentropic flow equations:

$$q = \frac{\gamma}{\gamma - 1} (k_p(P_{c1} - P_{c2}) + P_{c2}) \left\{ \left(\frac{k_q(P_{c1} - P_{c2})}{k_p(P_{c1} - P_{c2}) + P_{c2}} + 1 \right)^{\frac{\gamma-1}{\gamma}} - 1 \right\}$$

Where q is the dynamic pressure in the middle of the test section, γ is the heat capacity ratio and K_q , K_p are the calibration coefficients.

To avoid error accumulation, the differential pressure transducer only measures the difference between P_{c1} and P_{c2} instead of individual values at each port. Thus the absolute value of P_{c2} is unknown in the model wind tunnel, which leaves the theoretical solution inapplicable. A linear approximation between the dynamic pressure and the differential pressure is however established using Bernoulli's equation for incompressible flow:

$$q = \frac{1}{2} \rho u^2 = K_q (P_{c2} - P_{c1}) + K_p$$

The determination of K_q and K_p was done by measuring the dynamic pressure at the reference position using a Pitot-static probe. The probe was aligned with the longitudinal axis of the test section. The balance struts were removed and the balance chamber was sealed from the test section. The experiment setup is shown in figure 2.2 and the linear approximation fitted to the measurement results is shown in figure 2.3. K_p and K_q are found to be 0.04 and 0.9676 respectively. For steady still air field in the test section, the system measures a false dynamic pressure at 0.04 Pa due to the presence of the K_p . However, the corresponding airspeed is negligible.



Figure 2.2: Airspeed calibration setup

Linear regression of dynamic pressure in the test section

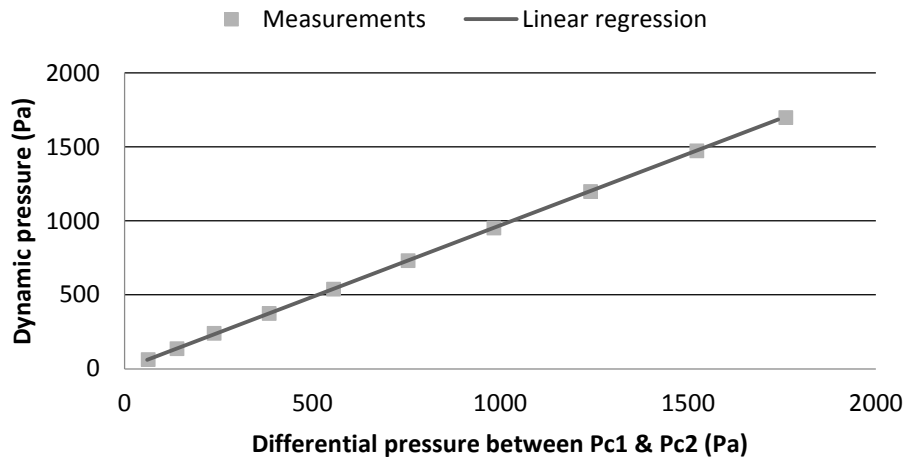


Figure 2.3: Airspeed calibration results

The flow quality regarding the stability of the airspeed was measured and the standard deviation was used to evaluate the variation of the airspeed for a given fan capacity.

$$\sigma = \sqrt{\frac{1}{N} \sum_{i=1}^N (x_i - \mu)^2}$$

Where $\mu = \frac{1}{N} \sum_{i=1}^N x_i$. The test airspeed was updated twice every second and the real-time airspeeds corresponding to different fan capacities were registered. 20 samples were taken for each fan capacity and the standard deviations from the mean value were given in figure 2.4.

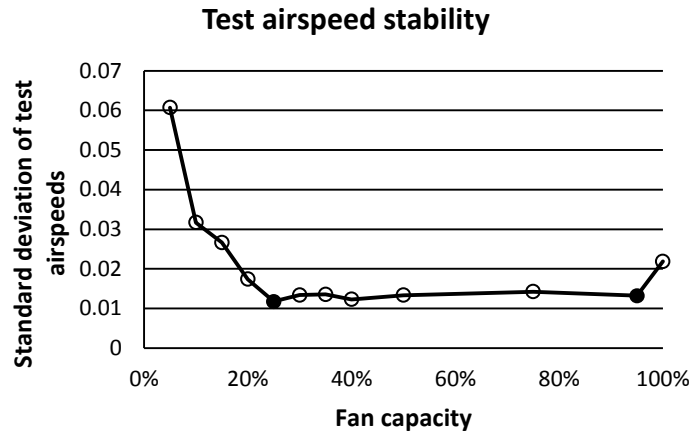


Figure 2.4: Airspeed stability with respect to fan capacity

The results indicate that the airspeed is less stable at low fan capacities. An increase in the standard deviation at maximum fan capacity is confirmed by monitoring the current and voltage across the motor. Unsteady behaviors observed in the motor electrical characteristics at top speed result in unsteady output torque transmitted to the fan, which leads to degradation of airspeed quality. The reason for such phenomenon is unknown and it is highly recommended that the capacity usage does not exceed 95% in order to prevent motor failure. The most accurate operating regime in terms of stability is between 25% and 95% (highlighted in solid dots in the diagram), corresponding to airspeed from 12.5m/s to 50m/s.

2.2. Boundary layer control system (BLC) study

2.2.1. Induced effects on flow quality by BLC

The boundary layer control system reduces the boundary layer thickness by creating a distributed low pressure area ahead of the test model. Due consideration must be given to the negative impacts on flow quality if the system is poorly designed. Such impacts include flow deflection, high pressure gradient and even asymmetric boundary layer profile in the lateral direction across the test section {5}.

2.2.2. Boundary layer measurements

The boundary layer theory indicates that the static pressure gradient inside the boundary layer is zero in the wall normal direction. With decaying streamwise velocity close to the wall, the total pressure inside the boundary layer will drop as shown by the definition of total pressure head:

$$P_{tot} = P_{stat} + \frac{1}{2} \rho u^2$$

Therefore, a total head rake can be used to capture the presence of the boundary layer. Using static pressure taps, the complete boundary layer velocity profile can then be determined. Two methods are employed to measure the boundary layer profile on the test floor with different emphases. Combined with the theoretical solution, method 1 delivers boundary layer profile with high accuracy and detailed boundary layer characteristics. Yet, the time-consuming nature of the method restricts the application to very few positions. By using the traversing gear, method 2 provides more flow information in the vicinity of the boundary layer in a larger lateral scale but suffers from uncertainties in tracing the probes' vertical positions.

The total head rake used in each method is a bank of Pitot tubes with sharp-edged entries. An accuracy interval of ± 4 degrees of flow inclination can be expected {6}. The flow can be assumed to be parallel to the probes' axis if the rake is aligned with the longitudinal axis of the test section since the test section flow angularity is within the accuracy interval.

Method 1

The boundary layer profile in the middle of the turntable was measured at test airspeed of 30 m/s. The total pressure distribution was measured by a total pressure rake, as shown in figure 2.5 and the static pressure was measured on the test floor at the center of the turntable using static pressure taps. To increase the space resolution in the wall normal direction, the rake was installed with 11.3 degree slope with respect to the test floor such that a displacement of 5 mm in the lateral direction will result in 1 mm space resolution in vertical direction, as shown in figure 2.6.

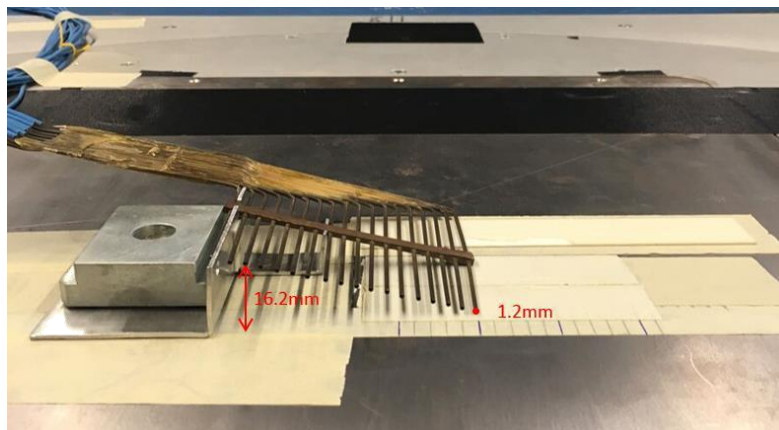


Figure 2.5: Rake installation

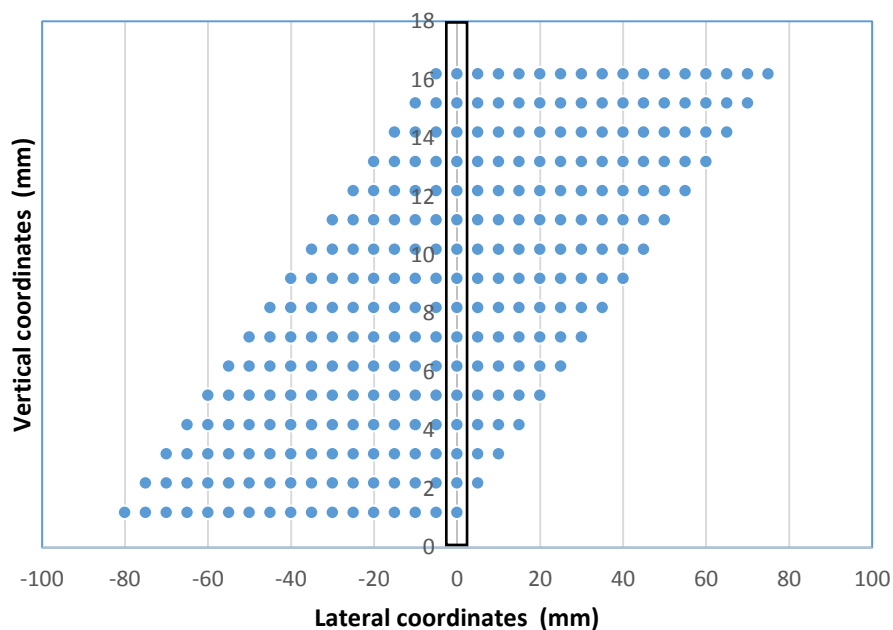


Figure 2.6: Rake traversing

15 trails are required for a complete boundary layer measurement in the center of the turntable. The measurement grids (highlighted in red box) cover the distance from 1.2 mm up to 16.2 mm above the

test floor. The measurement was performed for both BLC on and off. The corresponding streamwise velocity profiles are calculated as $u = \frac{2(P_{tot}-P_{stat})}{\rho}$ and the results are given in figure 2.7.

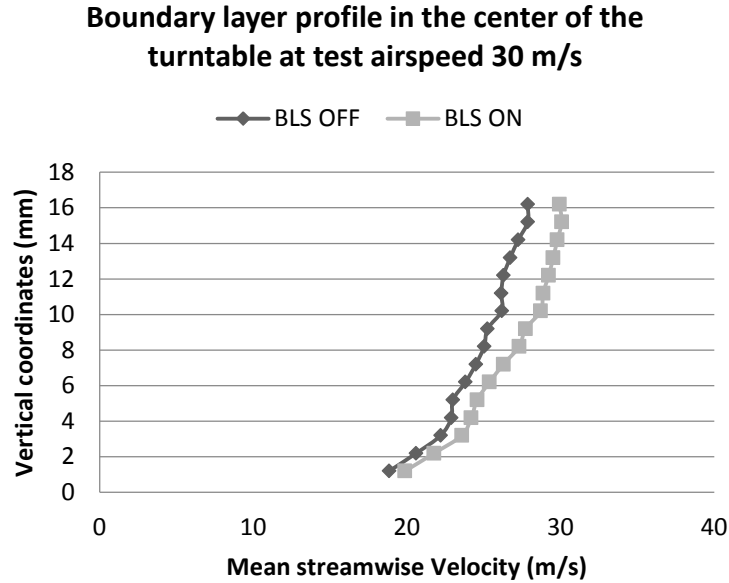


Figure 2.7: Boundary layer profile in the center of the turntable at test airspeed 30m/s

With the BLC system on, the boundary layer thickness is around 14.2mm. With the BLC system off, the current setup however could not capture the complete profile since the boundary layer thickness exceeds the top limit of 16.2 mm for the measurement grids. By applying linear interpolation within the range of the discrete set of data points together with the no-slip wall condition at the test floor, a rough velocity profile for the case with BLC on can be obtained, based on which the characteristics of the boundary layer can be determined in table 3.

Table 3: Boundary layer characteristics at test airspeed 30m/s with BLC on

Displacement thickness (mm)	$\delta_* = \int_0^\infty \left(1 - \frac{u(z)}{u_0}\right) dz$	2.2
Momentum loss thickness (mm)	$\theta = \int_0^\infty \frac{u(z)}{u_0} \left(1 - \frac{u(z)}{u_0}\right) dz$	1.5
Shape factor	$H = \frac{\delta_*}{\theta}$	1.47

Since the typical shape factor for a turbulent boundary layer is 1.3-1.4[7].The test floor boundary layer is turbulent. According to the turbulent boundary layer theory, the velocity profile outside of the laminar sub-layer can be described by the general log law.

$$\bar{u}(z) = \frac{2.3u_*}{\kappa} \log_{10}(z/z_0)$$

\bar{u} = mean streamwise velocity

u_* = shear velocity

κ = Von Karman constant

z_0 = characteristic roughness (dependent of the type of turbulent boundary layer)

z = wall normal coordinates

The logarithmic profile provides an estimation target to perform mathematical regression analyses. The regression function is:

$$\bar{u} = 4.2 \log_{10}(z) + 18.46$$

The mean streamwise velocity profile is given by figure 11 in linear scale and figure 12 in semi-log profile. The linear axes reveal the more familiar boundary layer profile. The semi-log scaled profile, however, is more informative since the characteristic roughness z_0 and the shear velocity u_* can be determined from the profile.

The characteristic roughness z_0 is given by the intersection point between the regression function and the y axis, as the mean streamwise velocity \bar{u} reaches zero as the wall normal coordinates equals to the characteristic roughness z_0 . The shear velocity can be determined by the slope of the regression function.

$$z_0 = 1.1 \times 10^{-2} \text{ (mm)}$$

$$u_* = \frac{\kappa}{2.3} \frac{\bar{u}_1 - \bar{u}_2}{\log_{10}(z_1/z_2)} = 0.73 \text{ (m/s)}$$

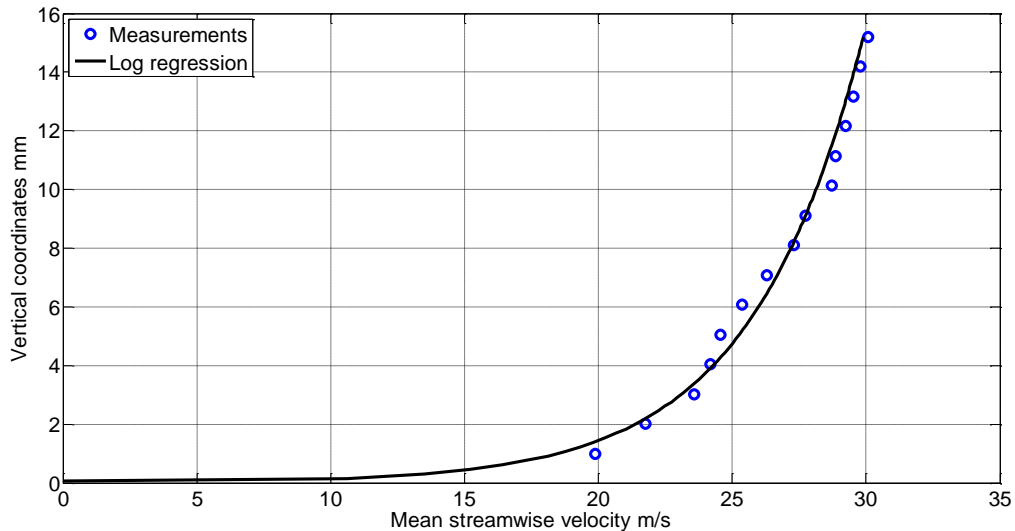


Figure 2.8: Boundary layer profile logarithmic regression in linear scale

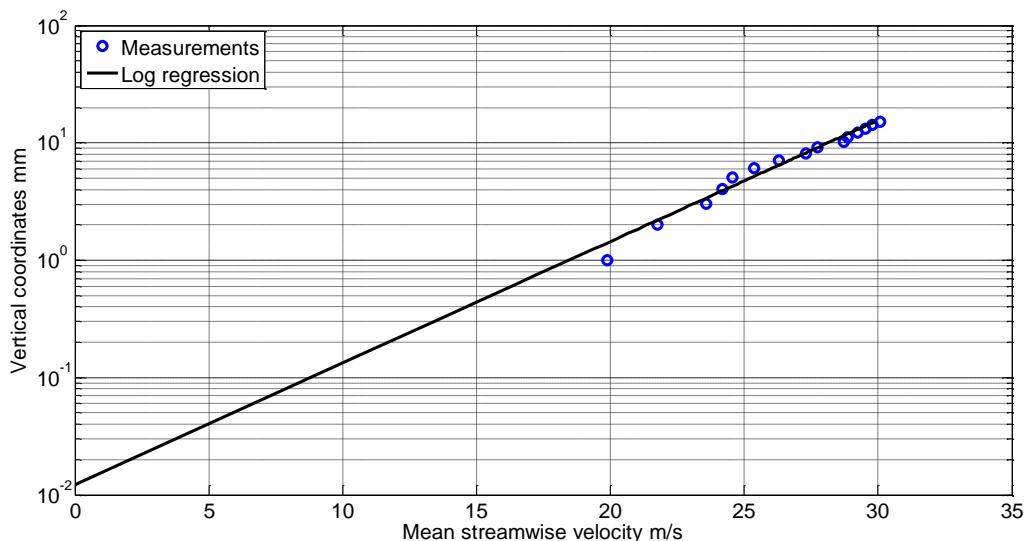


Figure 2.9: Boundary layer profile logarithmic regression in semi-log scale

Method 2

The boundary layer profile is measured in a larger scale compared to method 1. Utilizing the lateral traversing gear and the total head rake with increasing spatial density, a measurement plane across the middle of the turn table with dimensions of 400mm*103.5mm is defined. Since the measurement area is rather small compared to that of the test section, the static pressure over the measurement area is assumed to be constant and the value is measured at the center of the turntable. The experiment setup is shown in figure 2.10 where the red box represents the measurement plane.

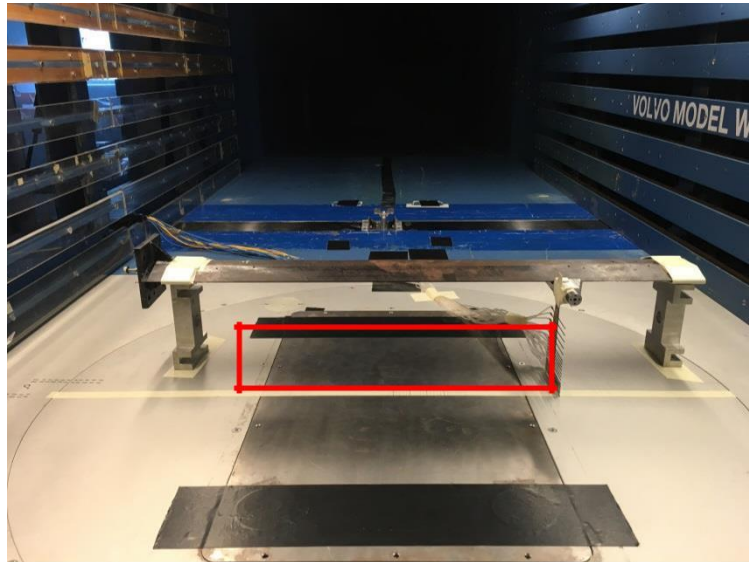


Figure 2.10: Traversing gear measurement area

The vertical coordinates of the probes must be monitored and measured carefully due to the difficulties in parallel alignment of the traversing gear with respect to the test floor. The vertical positions of the probes will change linearly with their lateral position on the rake if the traversing gear is mounted with a certain angle to the test ground. The accuracy of the measurements is sensitive to the vertical coordinates since the boundary layer thickness deviates rapidly with vertical distance from the test floor

The measurement was performed at test airspeed of 50m/s with and without BLC, the velocity profiles with actual measurement grids (highlighted in black dots) are given in figure 2.11 and figure 2.12.

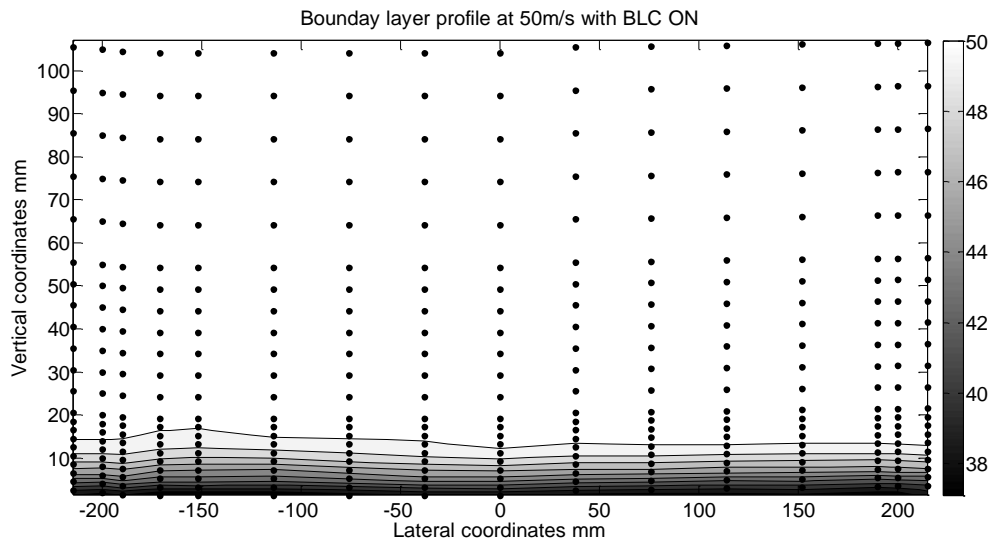


Figure 2.11: Boundary Layer profile with BLC at 50m/s

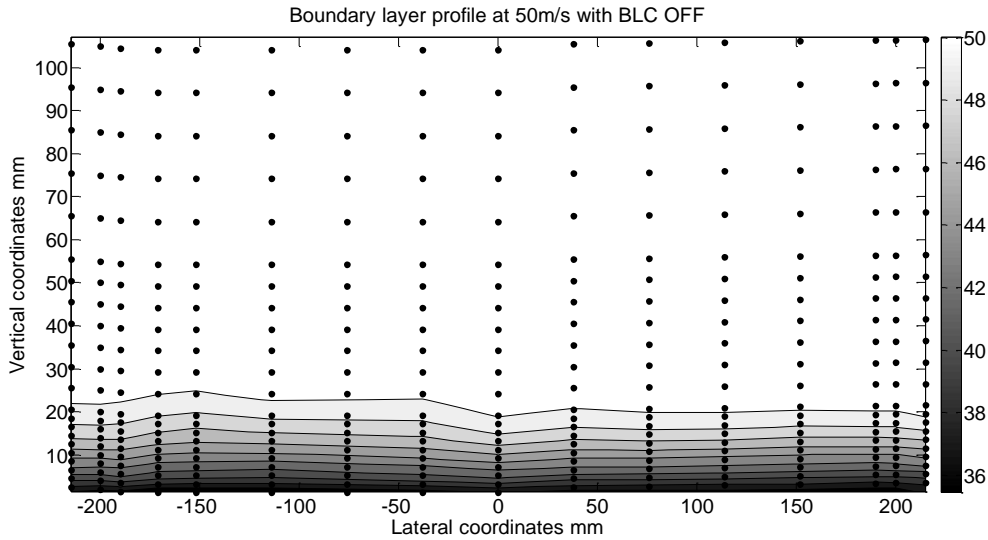


Figure 2.12: Boundary Layer profile without BLC at 50m/s

2.2.4 Boundary layer thickness prediction

The boundary layer developed on the test floor introduces major distortion to the vehicle underbody flow, which deviates from the actual on-road driving condition. Giving its tremendous impacts on the vehicle's measured aerodynamic performance, a boundary layer prediction model, customized for the wind tunnel tests, is established for resolving wind tunnel test floor interference related problem. The 99% boundary layer thickness for turbulent boundary layer on a flat plate can be estimated as:

$$\delta \approx 0.37x/Re_x^{1/5}$$

Where x is the distance from the leading edge and Re_x is the characteristic Reynolds's number based on x . It is possible to solve for the equivalent distance from the leading edge based on the boundary layer measurement discussed above despite the fact that no physical leading edge is presented in the test section. Yet it is not safe to generalize the concept of equivalent leading edge across the whole test section due to asymmetric flow behavior.

To predict the boundary layer thickness across the test section with high accuracy, the type of the turbulent boundary layer must be determined. The turbulent boundary layer can be roughly categorized into smooth and rough turbulent boundary layer as shown in figure 16.

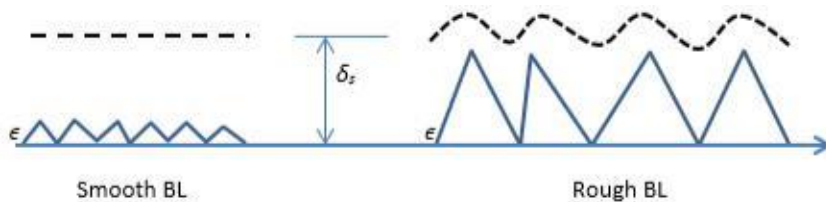


Figure 2.13: Turbulent boundary layer classification

The turbulent boundary layer is categorized by the relation between the surface roughness ϵ , and the laminar sub-layer thickness δ_s :

- If $\delta_s \gg \epsilon$, the turbulent boundary layer is smooth. The log region outside of the laminar sub-layer is hardly influenced by the surface texture on the wall. Thus the perturbation is confined in the viscous layer.
- Otherwise, the turbulent boundary layer is rough. The log region does feel the surface texture and the flow will be perturbed.

The velocities profile in the log region, through the characteristic roughness z_0 , varies with respect to the types of the boundary layer, as given in table 4{8}.

Table 4: Characteristic roughness for different types of turbulent BL

Turbulent BL type	Characteristic roughness
Smooth turbulent BL	$z_0 = f(u_*) = \frac{\nu}{9u_*}$
Rough turbulent BL	$z_0 = g(\epsilon) = \frac{\epsilon}{30}$

The type of the turbulent boundary layer can be determined by comparing the surface roughness against laminar sub-layer thickness estimated from the logarithmic regression profile mentioned before.

$$\bar{u} = 4.2 \log_{10} g(z) + 18.46$$

With shear velocity:

$$u_* = \frac{\kappa}{2.3} \frac{\bar{u}_1 - \bar{u}_2}{\log_{10}(z_1/z_2)} = 0.73 \text{ (m/s)}$$

This gives the laminar sub-layer thickness:

$$\delta_s = \frac{5\nu}{u_*} = 4.17 \times 10^{-2} \text{ (mm)}$$

The absolute surface roughness of the test floor is approximately 2×10^{-2} mm, which is of the same order of magnitude of the laminar sub-layer thickness. Hence the turbulent boundary layer measured at the center of the turn table is rough. However, the smooth turbulent boundary layer is assumed for predicting the boundary layer thickness for following reasons:

- The momentum transfer inside the turbulent boundary layer is strong enough to contain the low-energy fluid particle close to the wall {9} so that the perturbation caused by the surface texture can hardly travel to the outer edge of the boundary layer. The surface roughness has a huge impact on the skin friction but a relatively small impact on the boundary layer thickness.
- The surface roughness is not constant across the test floor and no method or equipment is available in the model wind tunnel to measure it with high accuracy. Thus the effect of surface roughness cannot be accurately quantified.
- By using the smooth boundary layer model, the surface roughness can be removed from the general log law, which leaves only one parameter to be determined, namely the shear velocity, u_* .

$$\bar{u} = \frac{4.2u_*}{\kappa} \log_{10} \left(\frac{9zu_*}{\nu} \right) + B$$

Where B is the correlation constant calculated from logarithmic regression profile. With the smooth boundary layer model and the correlation constant B, the shear velocity can be calculated given the mean streamwise velocity \bar{u} at certain height z inside the boundary layer. Thus the unique log profile at any position can be estimated after a one-point measurement. The model was validated at various wall normal positions inside the boundary layer against the logarithmic regression from the measurement results. The validation log profiles is shown in figure 2.14 & 2.15 and shear velocities for the most accurate validation is given by table 5

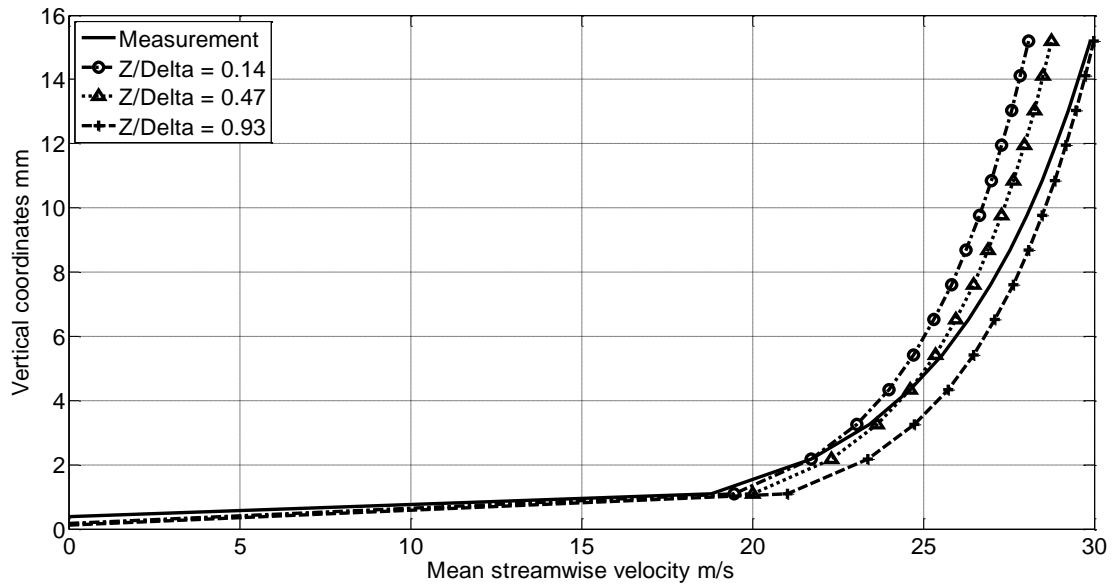


Figure 2.14: Velocity profiles for prediction model and measurement

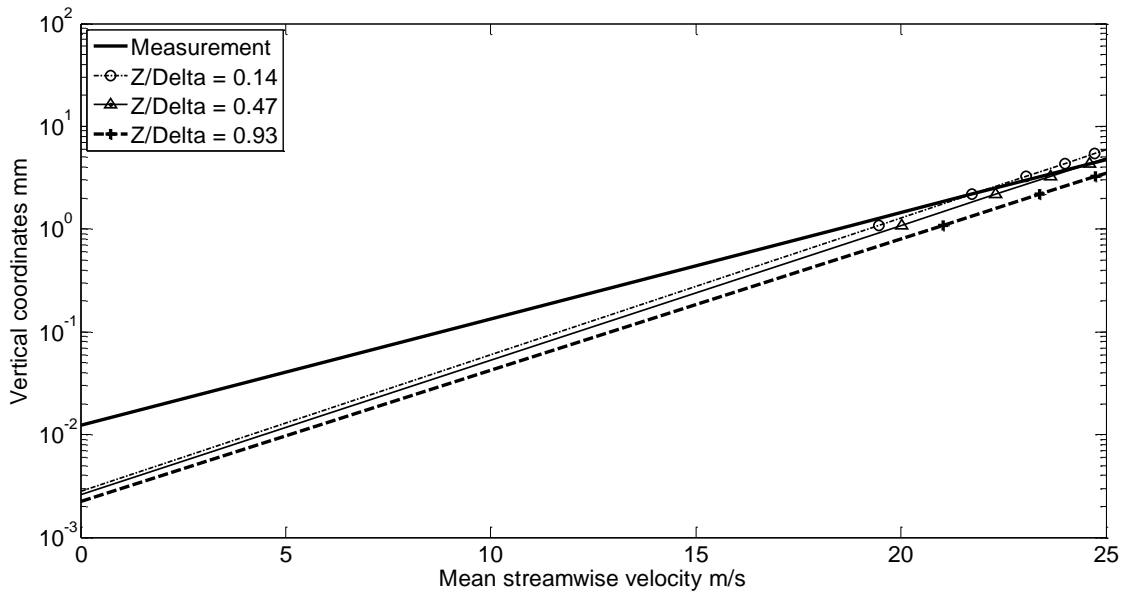


Figure 2.15: Velocity profiles for prediction model and measurement near the wall (semi-log)

Table 5: Shear velocities for prediction model and measurement

	Shear velocity u_* (m/s)
Generalized model	0.73
Measurement logarithmic regression	0.59

The wall normal position is normalized by the 99% boundary layer thickness (Δ). The accuracy regarding the boundary layer thickness improves as the acquisition point at which the model is evaluated approaches the outer edge of the true boundary layer. For a reasonable prediction, the normalized wall normal position of generalizing operation should be above 90 % of the boundary layer thickness.

The generalized model predicts the shear velocity with large discrepancy as shown in figure 2.15 and table 5. The predicted velocity profile deviates further from the measurement as it approaches the test floor. The prediction of the outer edge of the boundary layer is however rather accurate. The use of smooth boundary layer model can be justified as long as the main interest is to predict the boundary layer thickness.

2.3. Horizontal buoyancy

With the boundary layer development on the test floor, the effective jet area will be diminished. According to the mass flow conservation, the free stream airflow tends to accelerate toward the exit cone in an unobstructed wind tunnel. It follows that the static pressure will drop in the streamwise direction due to flow acceleration. This effect is illustrated in figure 2.16.

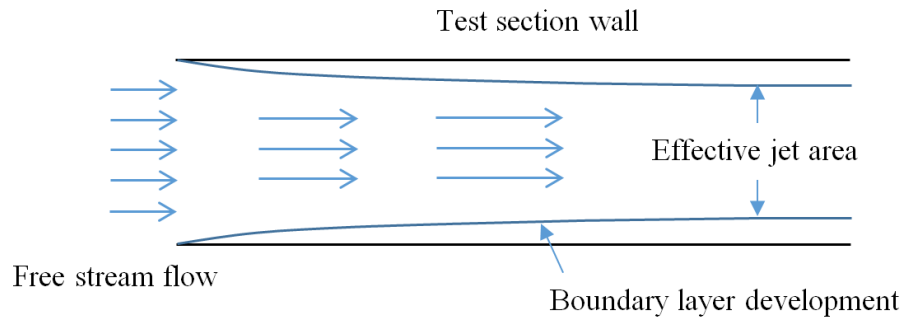


Figure 2.16: Flow acceleration due to boundary layer development

The flow acceleration produces an alteration to the normal static pressure distribution along the vehicle in the real road condition so that uncertainties in drag might be introduced to the tests. However, this effect is normally insignificant for test sections equipped with slotted walls. The resulting drag may be calculated as the integral of the product of differential static pressure and local cross sectional area of the model over the entire model length:

$$f_{buoyancy} = \int_0^l s_l \frac{dp}{dl} dl$$

- l : the distance from the nose of the test model.
- S_l : the cross sectional area of the model at station l
- p : the static pressure

The induced drag by horizontal buoyancy could be significant particularly for vehicles with low width to length ratio and special measures must be taken to evaluate this effect. This was done by measuring the static pressure variation along the oncoming flow in the unobstructed wind tunnel. Predrilled static pressure orifices on the second slot of the side wall (11.5 cm off the test floor) were scanned with and without BLC at constant airspeed. The measurements locations are given in figure 2.17.

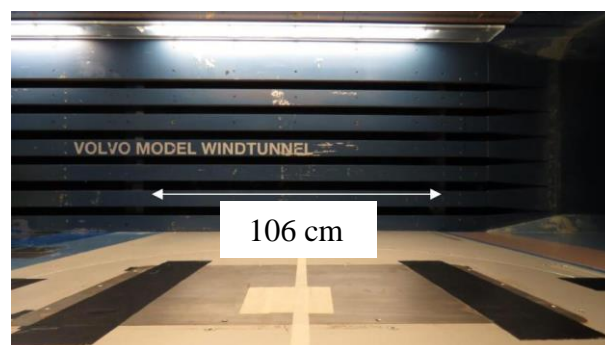


Figure 2.17: Static pressure measurements along the test Section

The static pressure is normalized by the dynamic pressure with respect to pc_2 . The variation of the static pressure coefficient with respect to streamwise coordinates is given in figure 20 where the mounting position of the test model is highlighted in solid lines.

$$cp = \frac{P_i - P_{c2}}{q}$$

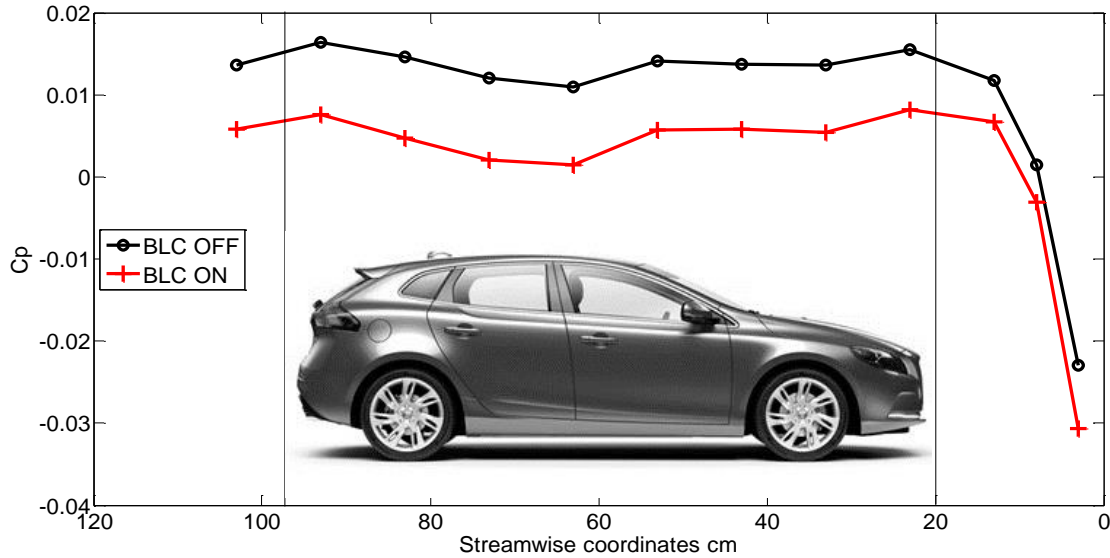


Figure 2.18: Static pressure distribution along the test section

Note that the measurements were carried out at same airspeed where the dynamic pressure and pc_2 are approximately identical. Thus the systematic deficiency in longitudinal static pressure for BLC on is due to total pressure losses introduced by boundary layer control system (Appendix). The local loss factor k can then be determined conveniently by the difference in the pressure coefficients [10]. The averaged loss factor over the model longitudinal length is found to be 0.01.

$$k = \frac{\Delta p}{q} = cp_{blc-off} - cp_{blc-on}$$

The resultant drag cannot be accurately determined without knowing the variation of the cross sectional area with respect to its length $\frac{dp}{dl}$. Yet a simplified method can be established to estimate the maximum drag due to horizontal buoyancy by considering the model as a 2D thin plate with its frontal area. Assuming the maximum differential static pressure measured in the region where the 3D model sits is applied completely on the 2D thin plate, the most extreme resultant drag is calculated as:

$$f_{buoyancy} = S_{front}(p_{max} - p_{min})$$

Taking the frontal area of model Aero 2020, the most extreme resultant drag is given by table 6. The influence on drag coefficient is negligible compared to the accuracy interval of the force measurements, thus no horizontal buoyancy correction will be applied.

Table 6: Maximum resultant drag due to horizontal buoyancy

Airspeed(m/s)	Induced drag(N)	Cd
30	0.448	0.000829
50	1.246	0.000830

3. Measurement quality

The measurement accuracy was determined by repeating a trail for 10 times under the same condition. These tests serve the purpose to examine the reproducible accuracy of the 6-componet balance, the yaw angle controller and the airspeed regulator. Yaw and Reynolds sweeps were performed on the Volvo aerodynamic reference model (as shown in figure 3.1 and 3.2), which is equipped with detachable back configurations, flat under body and fixed wheels.



Figure 3.1: Square back



Figure 3.2: Fastback

3.1. Reynolds Sweep Repeatability

10 trails of complete forces and moments measurements were done for each rear block configuration, which included drag (C_d), front axle lift (C_{lf}), rear axle lift (C_{lr}), front axle side force (C_{sf}), rear axle side force (C_{sr}), pitching moment (C_{pm}), yawing moments (C_{ym}) and rowing moments (C_{rm}). 600 samples were gathered at different airspeeds and the repeatability was monitored by determining the standard deviation from the mean values obtained for each trail. High repeatability is characterized by low standard deviation. The force measurement results for square back are given in figure 3.3 and fastback in figure 3.4.

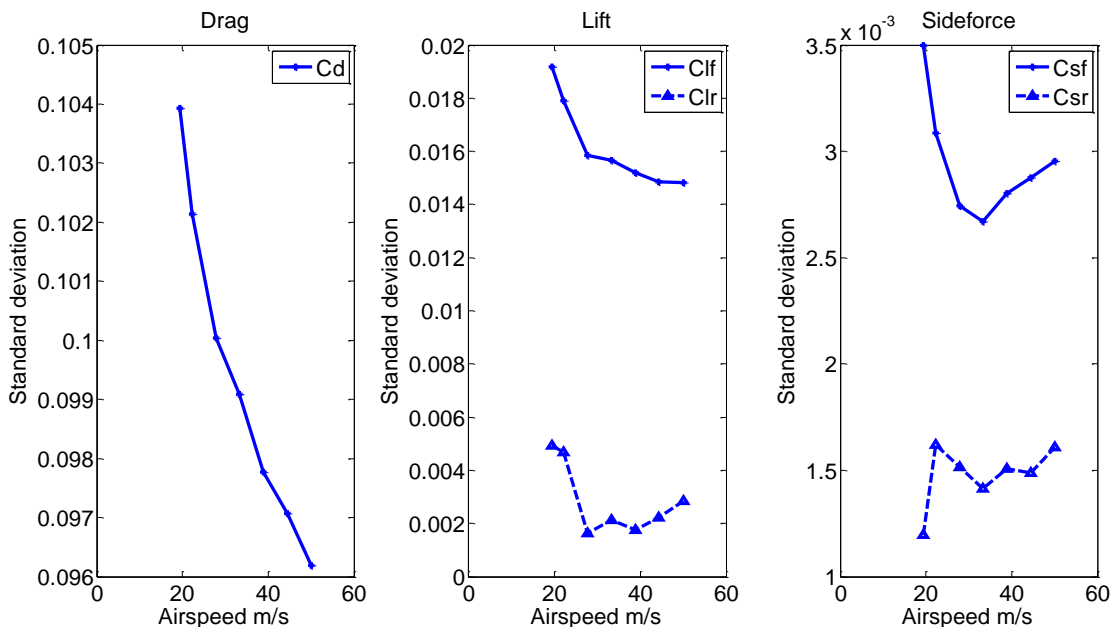


Figure 3.3: Airspeed dependence on repeatability for square back.

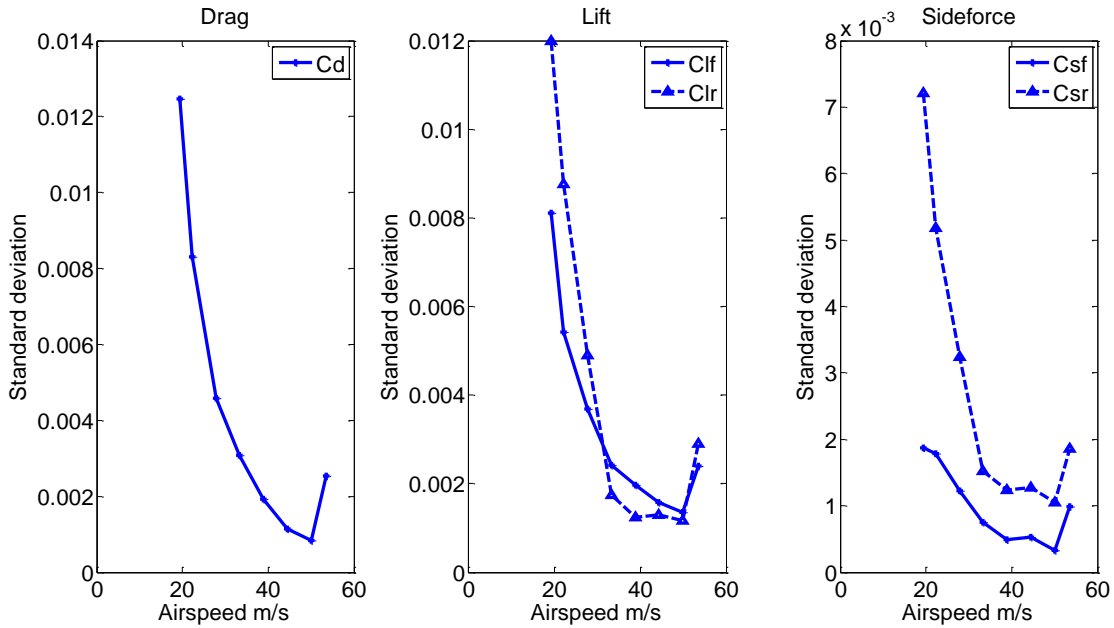


Figure 3.4: Airspeed dependence on repeatability for fastback

The repeatability for aerodynamic loads measurements is model dependent yet general conclusions can be drawn as follows:

- The repeatability for side force and moments measurements (see *Appendix 2*) is insensitive to airspeed variation when comparing the standard deviation magnitudes.
- Airspeed dependence can be neglected above 35 m/s as the standard deviation remains relatively constant for forces and moments.
- The most repeatable measurements for drag and lift are found to be at 50 m/s and an increase in standard deviation is observed when the airspeed approaches 53m/s, which can be explained by the instability of the electric motor (see *airspeed calibrations*).
- The maximum deviances in forces and moment coefficients of 10 trails at airspeed of 50m/s are given in table 7.

Table 7: Maximum Deviances in measurements at airspeed of 50m/s

	Cd	Clf	Clr	Csf	Csr	Cpm	Cym	Crn
Fastback	0.0028	0.0045	0.0040	0.0010	0.0039	0.0022	0.0016	0.0019
Square back	0.0022	0.0040	0.0030	0.0012	0.0021	0.0023	0.0006	0.0031

Even though the tests in a scaled wind tunnel should be run at as high a Reynolds number as possible to aid extrapolation to real driving conditions, the typical test airspeed is set to be 50m/s instead of top speed. This is justified considering durability and repeatability of the parameters of most interest, namely, drag and lift. The following tests were done at airspeed of 50 m/s unless stated otherwise.

3.2. Yaw sweep repeatability

The same procedure was applied at different yaw angles and the results for the square back setup are given in figure 3.5 and for the fastback setup in figure 3.6.

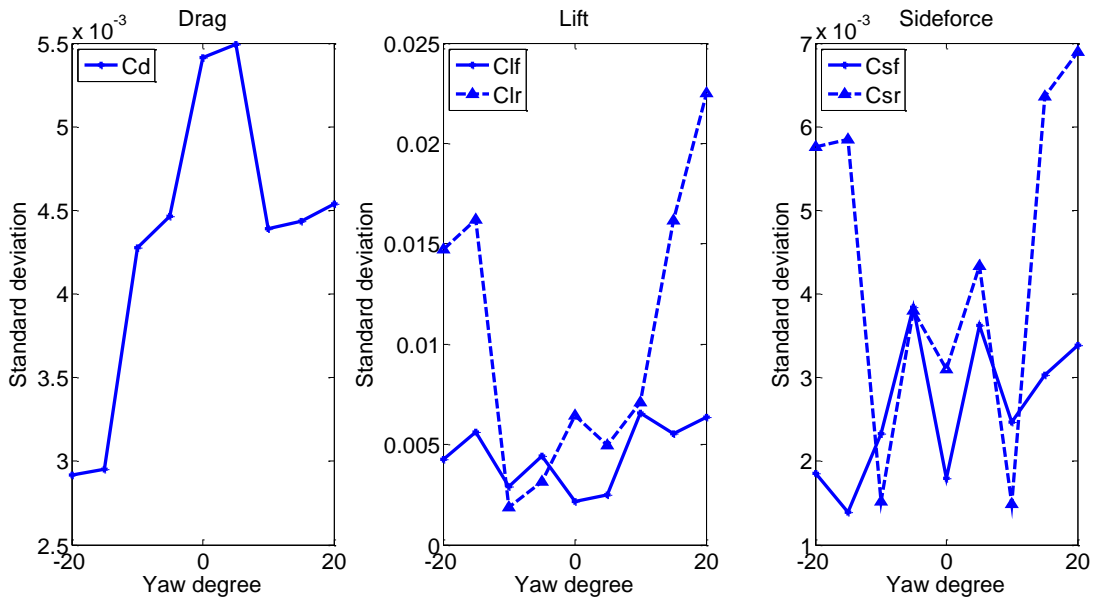


Figure 3.5: Yaw dependence on repeatability for square back

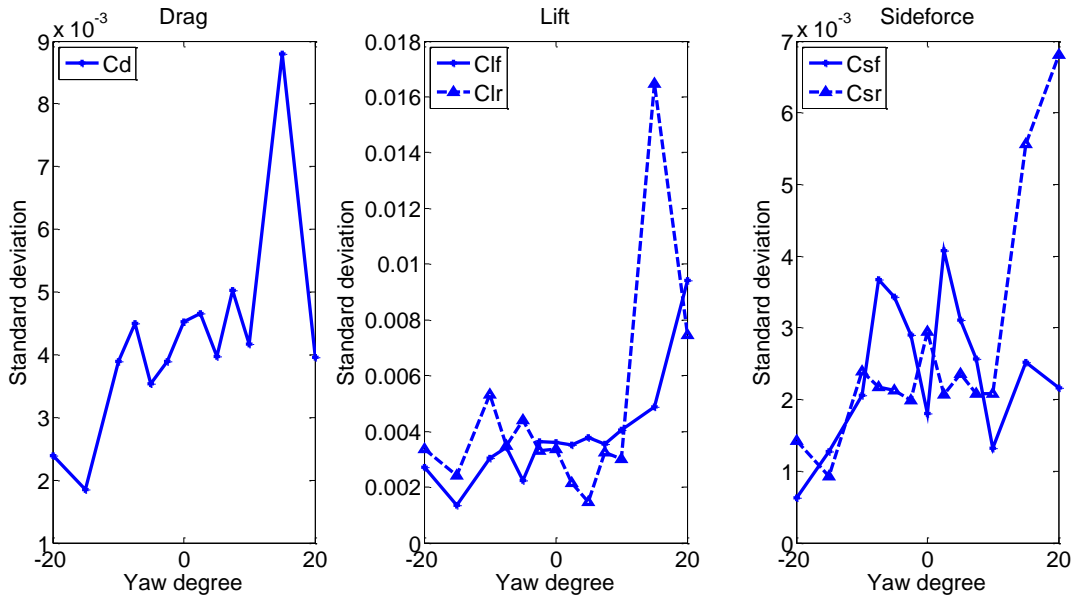


Figure 3.6: Yaw dependence on repeatability for fastback

The results show that:

- The most repeatable yaw sweep regime is bounded by ± 10 degrees. The turntable slips at higher yaw angles due to the severe increase in the yawing torque that overcomes the physical constraint between the turntable and the controlling motor. The target geometric yaw angle must be corrected by visual observation yet the correction is not consistent between each trail, which contributes to higher standard deviation above ± 10 degree.
- The maximum deviance in forces and moments coefficients of 10 trails at 15 and 5 degree yaw is given in table 8 for reference.
- The yaw sweep measurement is generally more repeatable than Reynolds sweep measurement since the airspeed is controlled manually while the yaw angle is changed automatically. Uncertainties are introduced in Reynolds sweep measurement due to the difficulties in achieving the same airspeeds.

Table 8: Maximum Deviances in measurements at 15° and 5° yaw

Yaw	Config	Cd	Clf	Clr	Csf	Csr	Cpm	Cym	Crm
15°	Fastback	0.0221	0.0131	0.0384	0.0062	0.0134	0.0198	0.0046	0.0176
	Square back	0.0143	0.0171	0.0515	0.0100	0.0207	0.0293	0.0076	0.0178
5°	Fastback	0.0102	0.0091	0.0038	0.0073	0.0057	0.0052	0.001	0.0098
	Square back	0.0170	0.0080	0.0170	0.0090	0.0122	0.0082	0.0030	0.0143

4. Correlation force measurement

Accurate values cannot be achieved in the model wind tunnel due to differences in the Reynolds number and tunnel-wall boundary layer development. However, correct trend predictions can be expected if the flow field in the scaled tunnel establishes similar behavior. To examine the transferability of model tests to full-scale test, the Aero 2020 was used as the reference model, as shown in figure 4.1 in full scale and figure 4.2 in 1/5th scale.



Figure 4.1: Full scale Aero 2020



Figure 4.2: 1/5th scale Aero 2020

4.1. Experimental setup

To fulfill the prerequisite of geometric similarity, the scale model was built as an exact replica of the full scale model with all primary details. Table 9 gives the description of the test models.

Table 9: Details of Full Scale and 1/5th Scale Clay Car

Full scale model	1/5 th scaled model
Flat underbody	Flat underbody
No side mirror	No side mirror
No cooling flow	No cooling flow
Angle adjustable diffuser angle	Angle adjustable diffuser angle
Height adjustable suspension	Height adjustable suspension
Real tires	Deformable tire with detailed tire bead
Moving belt	Rotating wheel system

The ride height during the test is defined to be the distance from the test floor to the fender lip and ground clearance is the distance from the test floor to the wheels. For the full scale model, the ride height was fixed when the model was mounted on the balance struts with the wheels contacting the test floor. While the ride height of the scaled model is determined by scale factor of 5 and the height of the suspension was adjusted for ground clearance of 2mm. For full scale model, the wheels were driven by the moving belts on the test floor. For scaled model, the rotating wheel system was activated for desired rotational speed.

Four configurations with geometric modifications which proved to yield aerodynamic benefits in the model wind tunnel were selected and manufactured to be tested in the full scale aerodynamic wind tunnel by Volvo aerodynamic validation group, as shown in figure 4.3 to figure 4.5.

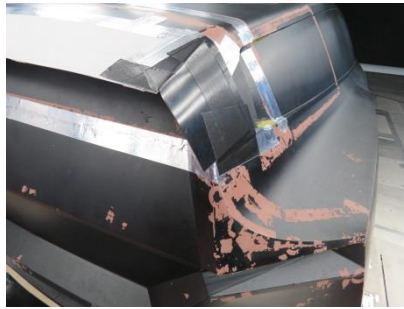


Figure 4.3: Rear roof wing extension

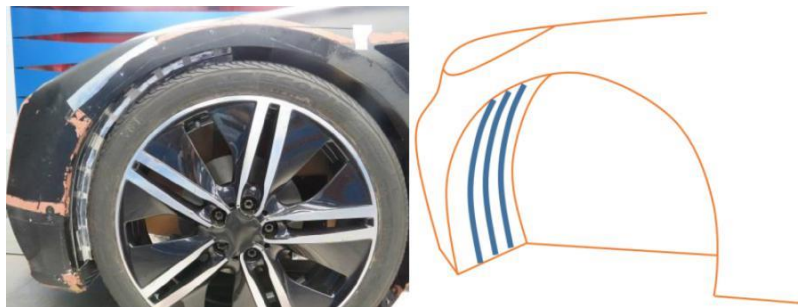


Figure 4.4: Front wheel bay ribs

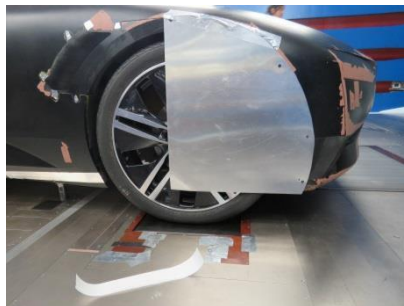


Figure 4.5: Front wheel cover

Configuration 1: The rear roof wing was extended to delay flow separation and thus reduce the wake size.

Configuration 2: Ribs with rectangular cross sections were installed in the front wheelhouse in order to stabilize the wheelhouse flow and thus reduce the drag

Configuration 3: The front wheelhouse was covered to block the air flow from entering in order to reduce the drag.

4.2. Trend prediction

For incompressible flow, the flow field around the 1/5 scale and the full scale model will be similar if the Reynolds numbers in both cases are equal. The Reynolds law of similarity requires the products of the test airspeeds and characteristic lengths of the model to be the same, according to the definition:

$$Re = \frac{V_{\infty} l}{\nu}$$

Where the kinematic viscosity of the air ν is usually assumed to be constant as its variation with respect to temperature range of 15° to 30° is negligible.

The typical test airspeed in the full scale wind tunnel is 38.8m/s, which would require test airspeed of 194m/s in the model wind tunnel to fulfill the similarity requirement of matching the Reynolds numbers. Thus the Reynolds law of similarity was not maintained here due to speed limitation. The transition from laminar to turbulent boundary layer is fed by the Reynolds number. The turbulent boundary can sustain greater adverse pressure gradient without separation, a brief delay in flow separation would result significant drag reduction for ground vehicles. Since the transition point for the full scale model is unknown, no boundary layer tripping was applied in the 1/5th model. However, the drag measurements demonstrate minor Reynolds effect as confirmed by yaw sweep tests on configuration 1.

The tests in the full scale wind tunnel (PVT) are carried out at 140 km/h, while the tests in the 1/5th model wind tunnel (MWT) are done at airspeeds of 140 km/h and 180 km/h. The reference value is taken to be the drag coefficient measured at full scale wind tunnel at 140km/h and zero yaw. The differential drag coefficients are shown in figure 4.6.

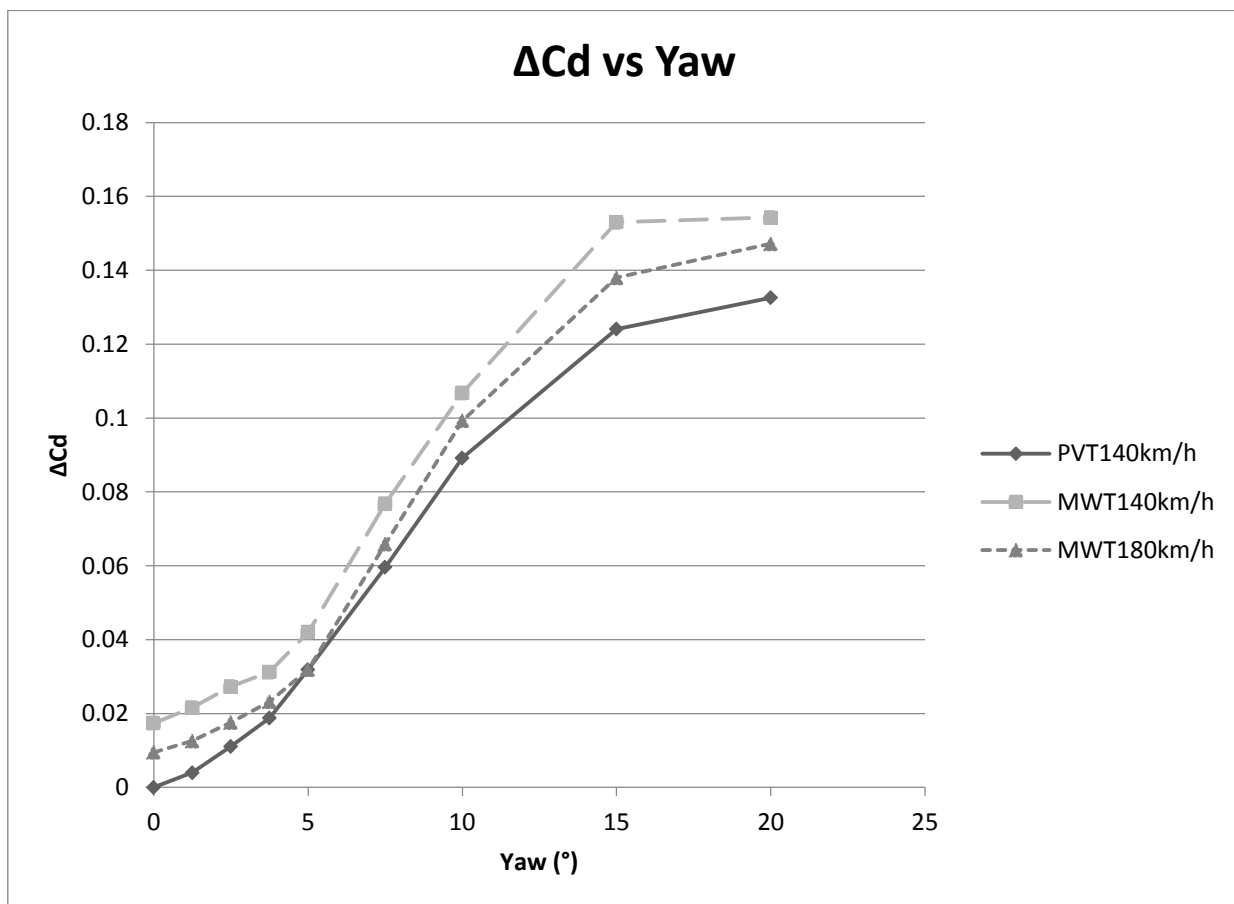


Figure 4.6: Reynolds number extrapolation effect

The results of the 1/5th model and the full scale tests generally share similar behaviors with a minor offset. One-quarter of Reynolds number in full scale test is achieved by airspeed at 180km/h in scaled test, at which the results are found to be more accurate in terms of trend prediction. Therefore further correlation tests in the model wind tunnel will be carried out at 180km/h as the most representative test airspeed to typical full scale tests. Yet the trend predictions for the non-dimensional force coefficients with respect to yaw angle are not always correct, since the Reynolds number is not the single dominant factor in wind tunnel tests. The following example shows serious discrepancies in lift force prediction. Figure 4.7 and 4.8 give the comparison results for front and rear axle lift coefficients acquired at 180km/h in the model wind tunnel and 140km/h in the full scale tunnel. The reference values are taken at full scale tests with zero yaw.

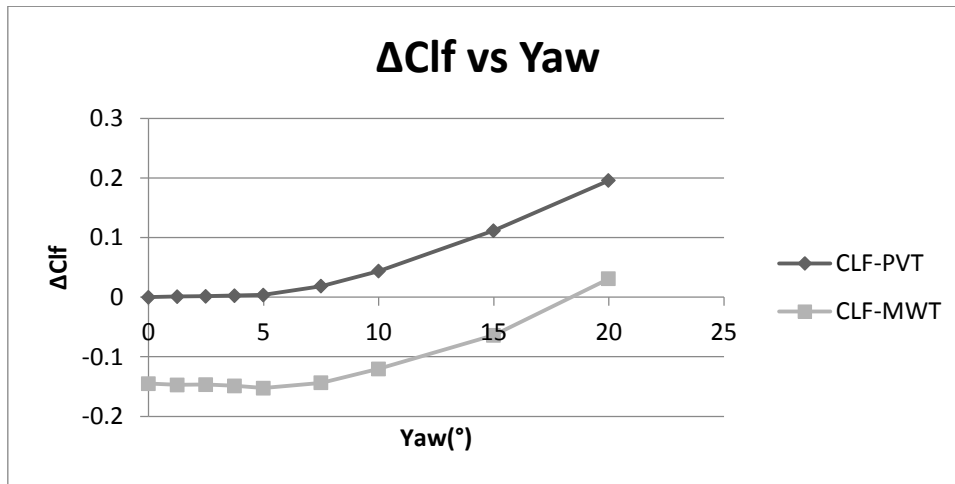


Figure 4.7: Comparison of differential front axle lift coefficients for scaled and full scale tests

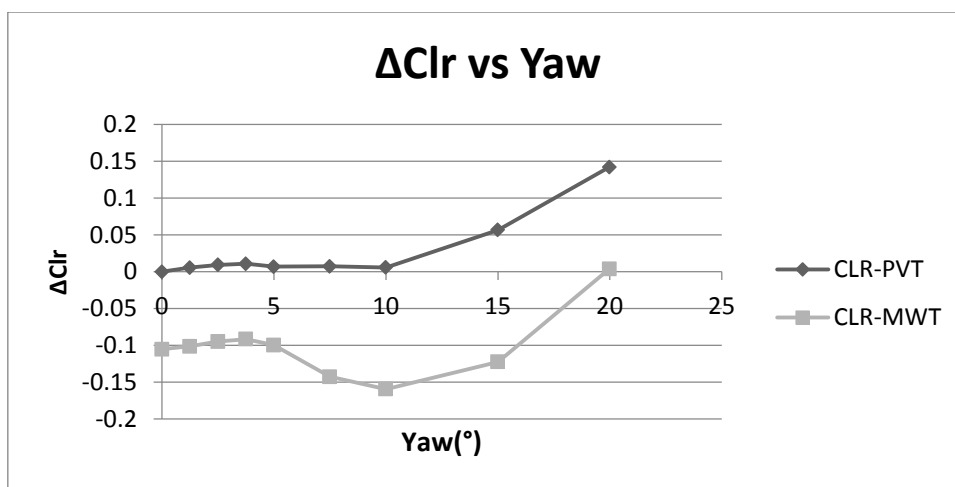


Figure 4.8: Comparison of differential rear axle lift coefficients for scaled and full scale tests

The model wind tunnel tests are generally incapable of predicting the correct values for the lift. Accurate trend prediction can be obtained for front axle lift but it is confined within 0-5 degrees for rear axle lift. The possible reasons for inaccurate characteristic and trend prediction in model wind tunnel tests are given below:

- The ground clearance in the scaled tests is one of the dominant factors that determine the lift characteristics. Flow acceleration through the narrow gap reduces the static pressures between the wheels and the test floor as the wheels are lifted above the ground, which contribute to negative lift (down force) on the test model. The Static pressure in this region decreases sharply as the ground clearance is reduced. Once the ground clearance reaches zero, the stagnation pressure is reached by the contact patch of the tires, the vertical component of which tremendously increases the positive lift {11}.
- The flow will be deflected as the test vehicle is yawed and flow separation along the test section walls may occur at high yaw angles {12}. Differences in the flow deflection between scaled and full scale tunnel could be held partly accountable for the incorrect trend prediction. The airflow is suspected of separating along the test section walls since the reduction in rear axle lift between 3.75 and 10 degree violates the typical lift-yaw curve for passenger cars.

4.3. Differential force prediction

The differential force and moment coefficients for different geometrical modifications are calculated figure 4.8 shows the differential drag coefficient in scaled and full scale tests calculated from corresponding baseline measurements.

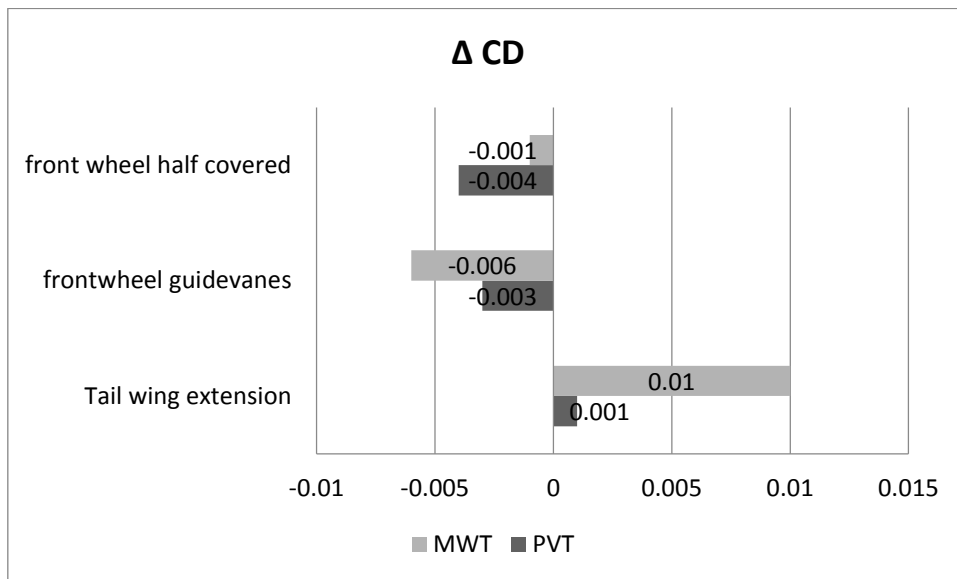


Figure 4.9: Differential Cd Comparison of Full scale and 1/5th Car

The drag prediction for scaled tests follows a similar trend as the full scale wind tunnel. The results are of same order of magnitude for the first two configurations. However the results for the last configuration demonstrate large discrepancies in the magnitude.

The comparison results for front and rear axle differential lift coefficients are given in figure 4.9 and 4.10.

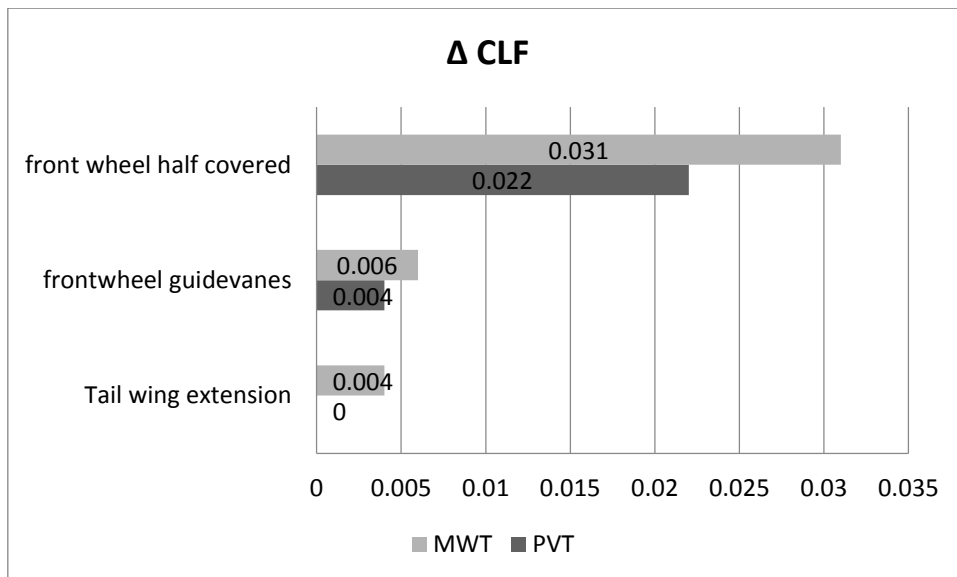


Figure 4.10: Differential Clf Comparison of Full Scale and 1/5th Scale Car

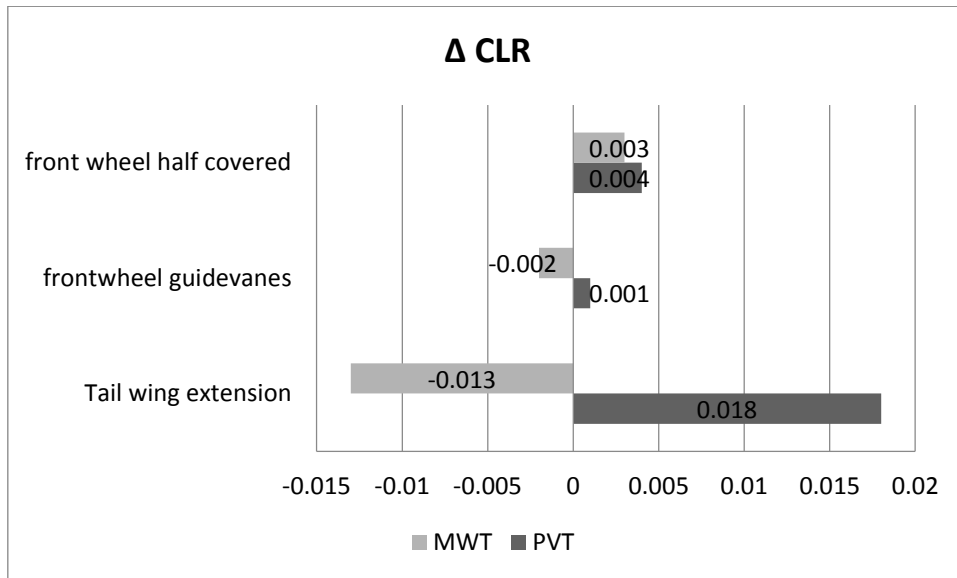


Figure 4.11: Differential Clr Comparison of Full Scale and 1/5th Scale Car

The scaled tests generally overestimate the differential front axle lift as seen in figure. It is worth noticing that neither the differential rear axle lift (figure 4.10) nor its yaw sweep variation (figure 4.7) can be trusted, reasonable prediction in lift can be expected as zero ground clearance is achieved.

5. Correlation unsteady base pressure measurement

The energy loss caused by the separated flow in the near wake region is one of the main contributions to the aerodynamic drag on ground vehicles. The unsteady base pressure measurements serve the purpose of analyzing the periodic oscillations in the pressure field, thus the critical geometric features influential in the near wake behavior can be identified. Different unsteady aerodynamic phenomena are characterized by the Strouhal number, which is defined in terms of characteristic length of the vehicle (square root of the frontal area), free stream velocity V_∞ and the characteristic frequency f .

$$St = f \frac{\sqrt{\text{Frontal Area}}}{V_\infty}$$

Previous studies indicate that the critical frequency range for full-scale vehicle dynamics lies between 0.5Hz and 4Hz [13], as shown in figure 5.1.

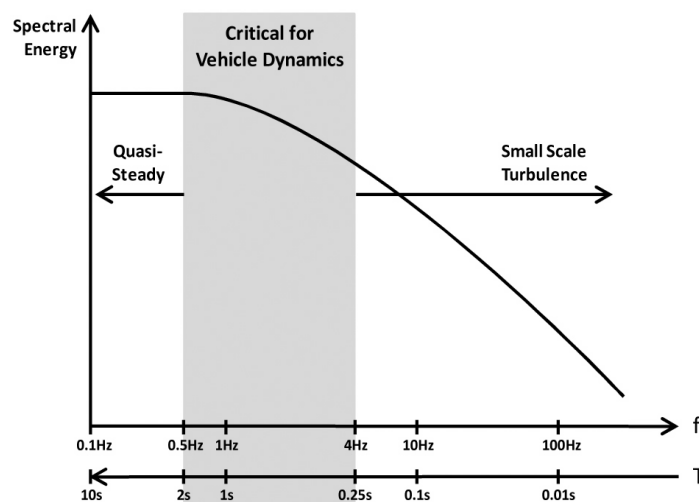


Fig 5.1: Critical frequency range for full-scale vehicle dynamics

Due to the scaling effect, the critical frequency range for a 1/5th scaled model would be amplified and lies within 2.5Hz and 20Hz.

The power spectral density of each pressure signal sequence was calculated to reveal the frequency content.

$$\rho_{xx} = \frac{\overline{p(t)p(t')}}{\overline{p^2}}$$

$$S_{xx}(\omega) = \frac{1}{2} \int_{-\infty}^{+\infty} e^{-iT'\omega} \rho_{xx}(T') dT'$$

Where ρ is the autocorrelation function and p is the static pressure.

A false peak will emerge due to the discontinuity at the cut-off frequency. Therefore, a high pass filter (Sinc filter) of 0.0001 Hz was applied to avoid the false peak from falling into the critical frequency domain. A single-window FFT cannot guarantee that the estimate of the power in a given frequency band is converged, so an average-based Welch's method is used. The pressure signals are divided into overlapping windows (Hanning window), the PSDs for each window are computed and then averaged together.

The proper orthogonal decomposition (POD) was used to obtain approximate descriptions for large-scale turbulent structures. It yields a set of empirical Eigen functions, where the Eigenvalue reflects relative energy or variance associated with corresponding mode. The energy represents the contribution of the corresponding mode to the turbulence field, thus the most energetic mode indicates the dominant flow structure. Details of the POD analysis are contained in ref {14}.

5.1. Experimental Setup

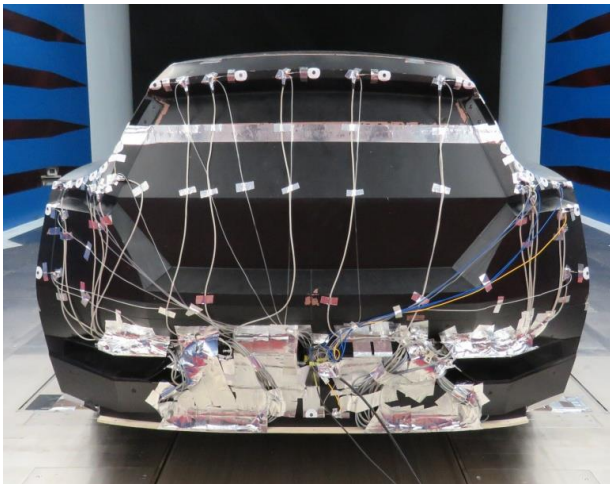


Fig 5.2: Pressure sensors on full scale car

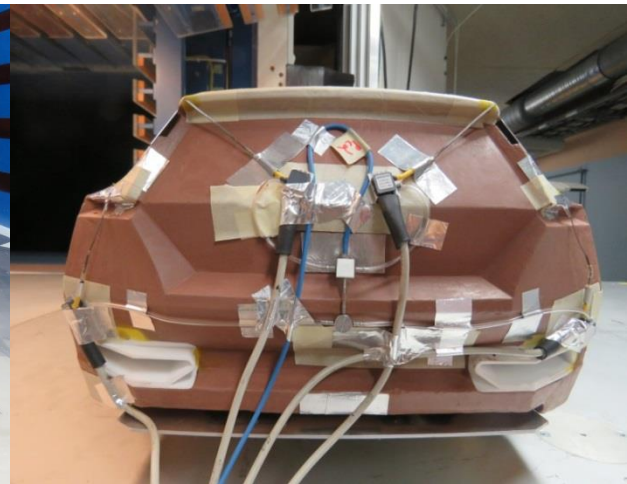


Fig 5.3: Pressure sensors on model car

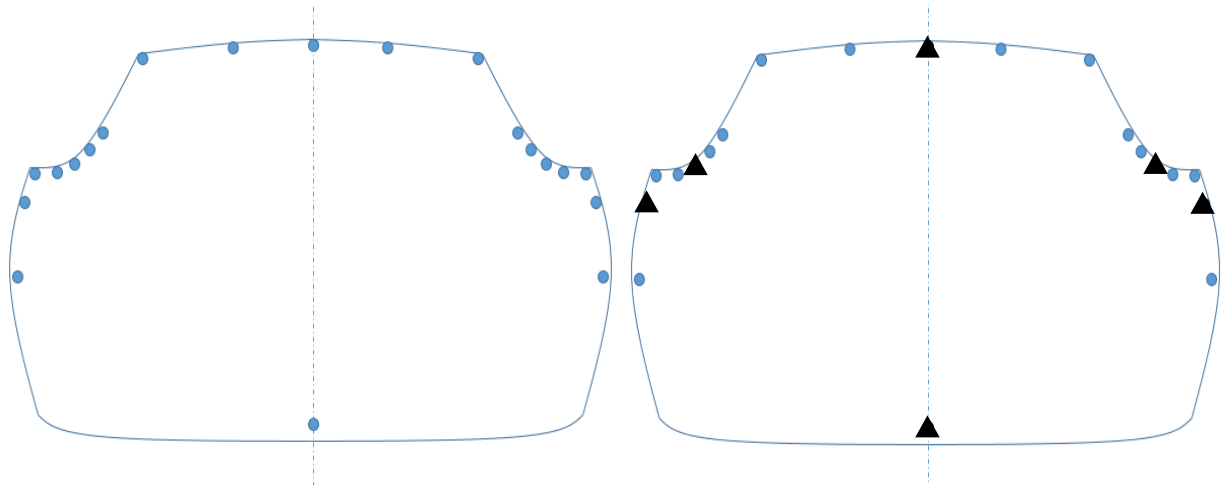


Fig 5.4: Sensors locations on full scale car

Fig 5.5: Sensors locations on model car

To limit the geometrical alteration due to the presences of the sensors and pressure transducers, the sensors were placed only in critical locations as shown in fig 5.4 and 5.5. Due to limitation in space on the scaled model, only 6 measurement positions were selected instead of 20 on the full scale. All measurements were sampled at 500 Hz and were taken for duration of 495 ± 15 s on the baseline with test airspeed of 180km/h and 0° yaw. Two configurations were tested in both tunnels: boundary layer control systems on and off.

5.2. Results for full scale tests

Low-frequency activities in the near wake region were identified using POD:

- Periodic fluctuation in the free stagnation point, also known as the wake pumping effect.
- Vortex shedding mode developed on the roof and underbody of the model.
- Vortex shedding mode developed on the right and left sides of the body, also known as the wake flapping effect.

However, due to complex flow behavior in the near wake region of the test vehicle, no specific peak was obtained in the power spectrum between 0.5Hz and 5Hz except one plateau around 1.5Hz. The corresponding Strouhal number is 0.043, which may be attributed to the wake pumping effect observed by Berger et al at a Strouhal number of 0.05 {15}.

5.2.1. Wake pumping mode

Duell et al {15} indicated that the pumping phenomenon derives from the pairing of vortices shed from the model edges where the model boundary layer separates from the body. Pairing continues until the shear layers from all sides coalesced at the free stagnation point. This periodic pumping moves the free stagnation point in the streamwise direction and results in periodic base pressure fluctuations. The effect of free stagnation point pumping on the upper and lower parts of the trapped ring-type vortex is shown in figure 5.6.

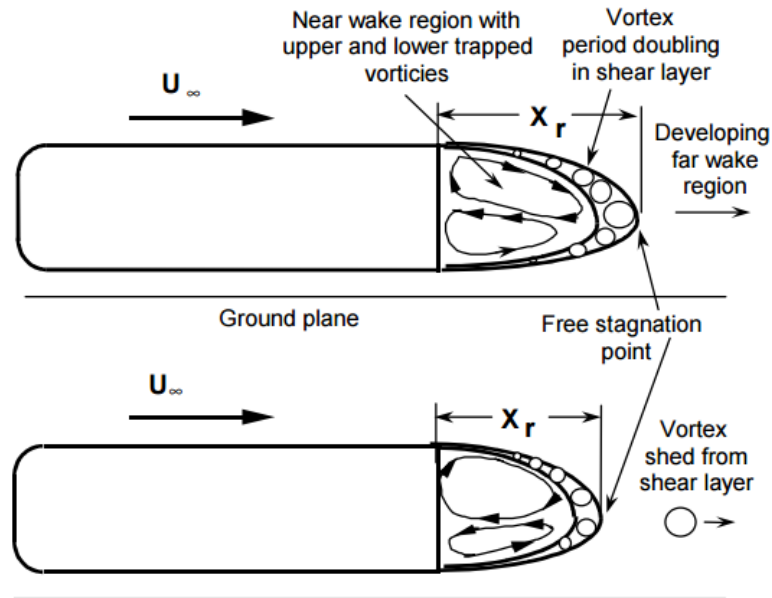


Figure 5.6: Free stagnation point fluctuation in longitudinal direction {15}

16 Eigen functions were obtained from POD analysis where mode 4 represented the universal symmetric phenomenon of wake pumping with an energy intensity of 8.8%. The aspect of the corresponding eigenvectors is shown in figure 5.7 by representing them in the form of cartographies on the rear of the model. The POD coefficient was plotted using color map where different gray scale represents anti-correlation, et cetera.

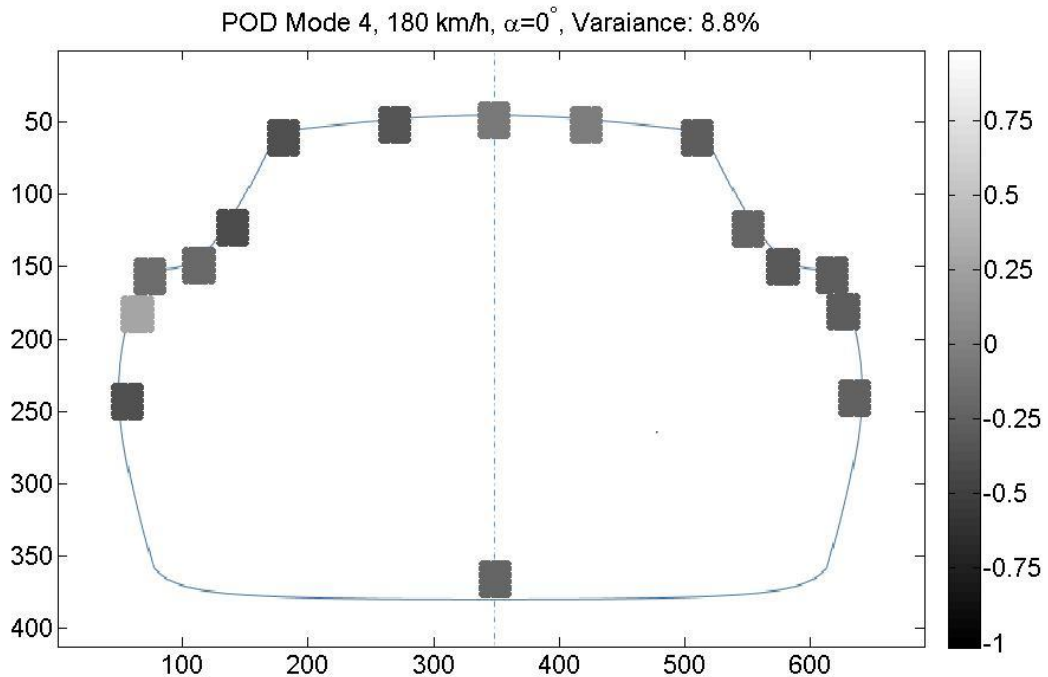


Fig 5.7: POD Mode 4-wake pumping

5.2.2. Vortex shedding modes

The vortices shed from the model edges can be roughly decomposed into modes in vertical and horizontal directions. Vortex shedding mode developed on the right and left sides of the body, also known as the wake flapping effect, was identified by the 1st POD mode containing a maximum energy intensity of 29.4%, which corresponds to the most dominating flow phenomenon. The POD coefficient is shown in figure 5.8 with a clear a left-to-right asymmetry behavior.

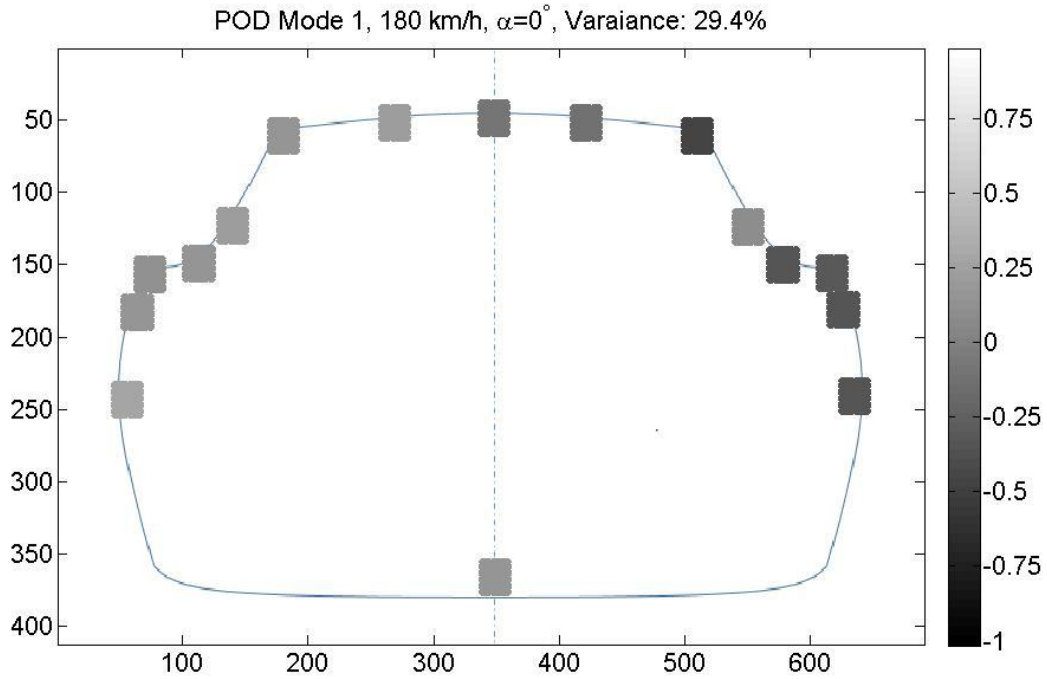


Fig 5.8: POD Mode 1-wake flapping

Trapped vortices developed on the roof and underbody of the model was identified by the 2nd POD mode containing an energy intensity of 29.4%. The POD coefficient is shown in figure 5.9 with a clear a top-to-bottom asymmetry behavior.

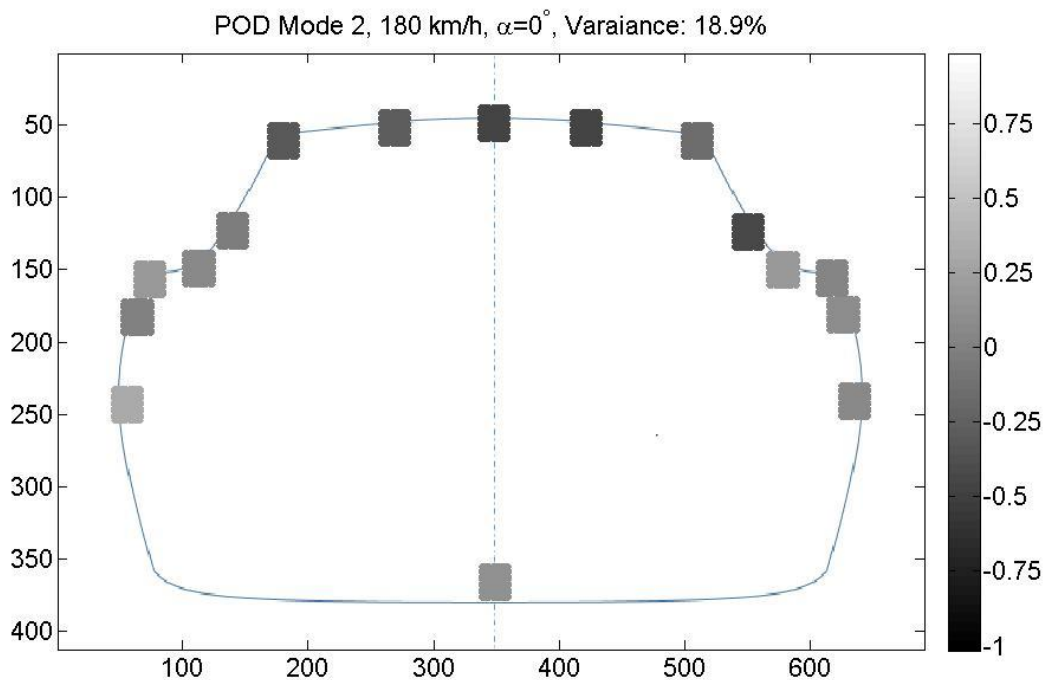


Fig 5.9: POD Mode 2-trapped Vortex

5.2.3. Wake center

POD analysis showed that the most dominating phenomenon in the near wake region is wake flapping. This is confirmed by determining the wake barycenter {16}. The base is divided into three regions, as shown in figure 5.10, in order to identify the geometrical features that have major impacts on the near wake. The wake center is defined as the pressure weighted center in lateral and vertical coordinates relative to the geometrical center of each region, given as:

$$X = \frac{\sum P_i X_i}{\sum X_i} \quad Y = \frac{\sum P_i Y_i}{\sum Y_i}$$

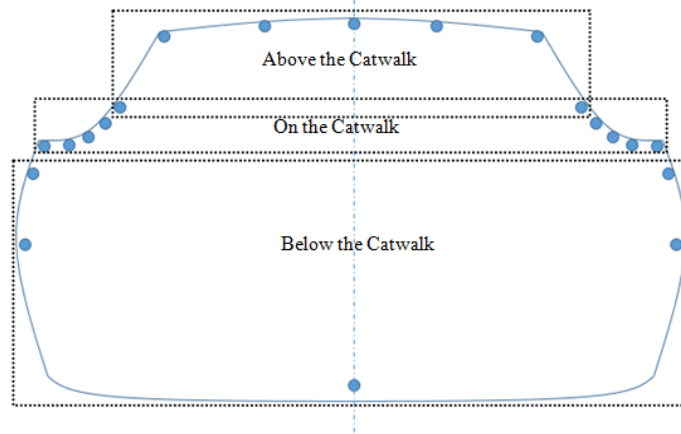


Fig 5.10: Regions of interest for wake center determination

The histograms of each wake center are given in figure 5.11 for lateral distribution and figure 5.12 for vertical distribution.

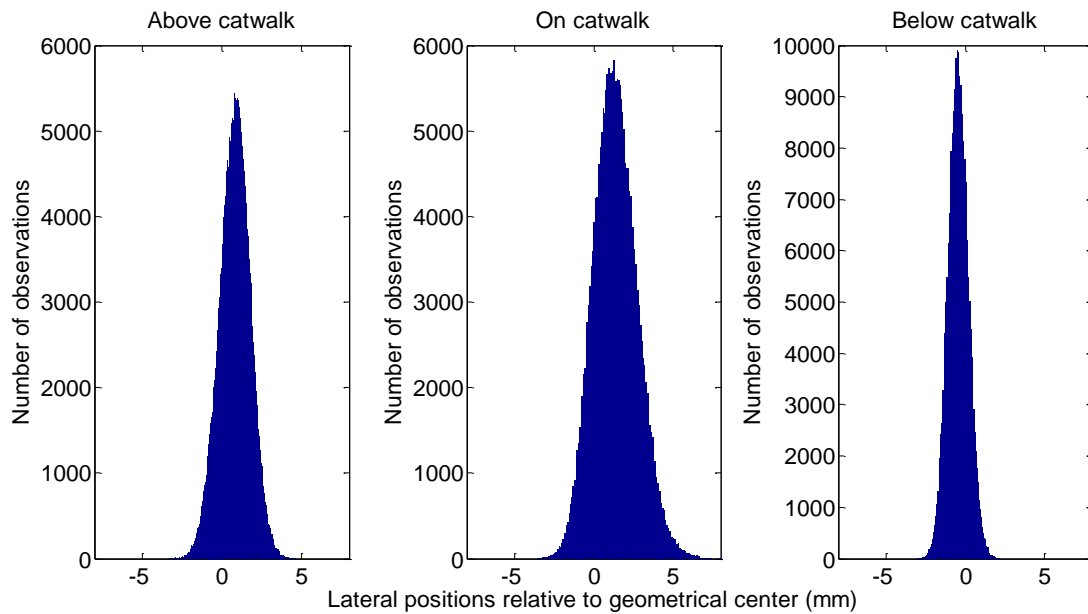


Fig 5.11: Lateral distributions of wake centers at three regions

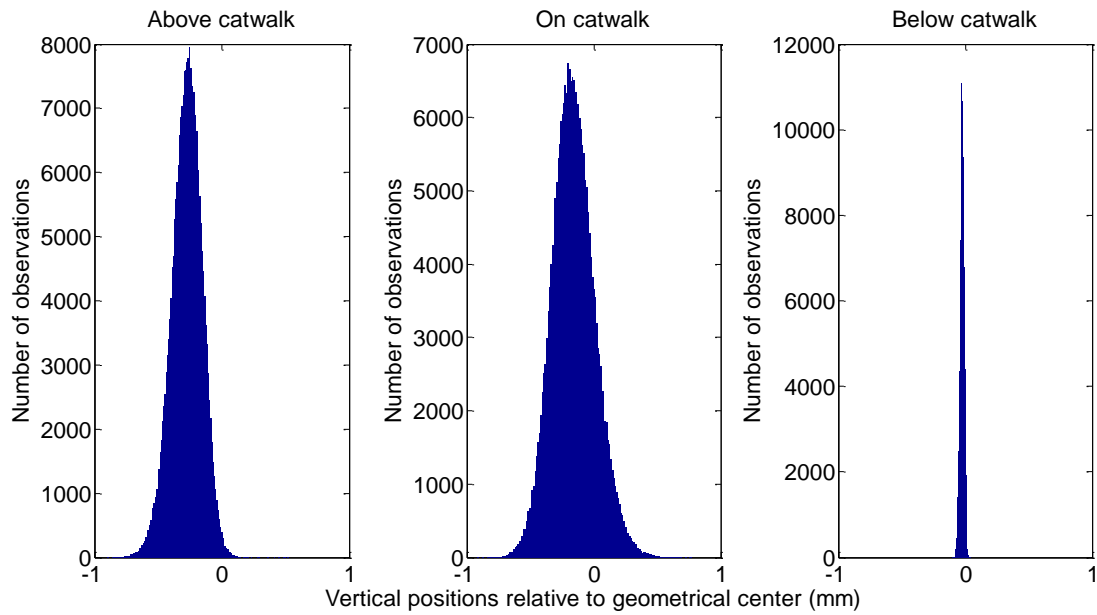


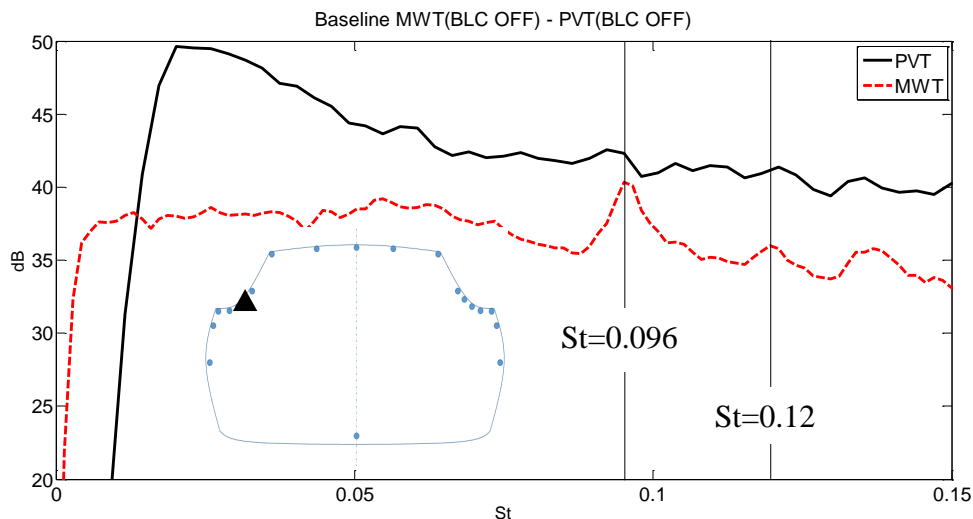
Fig 5.12: Vertical distributions of wake centers at three regions

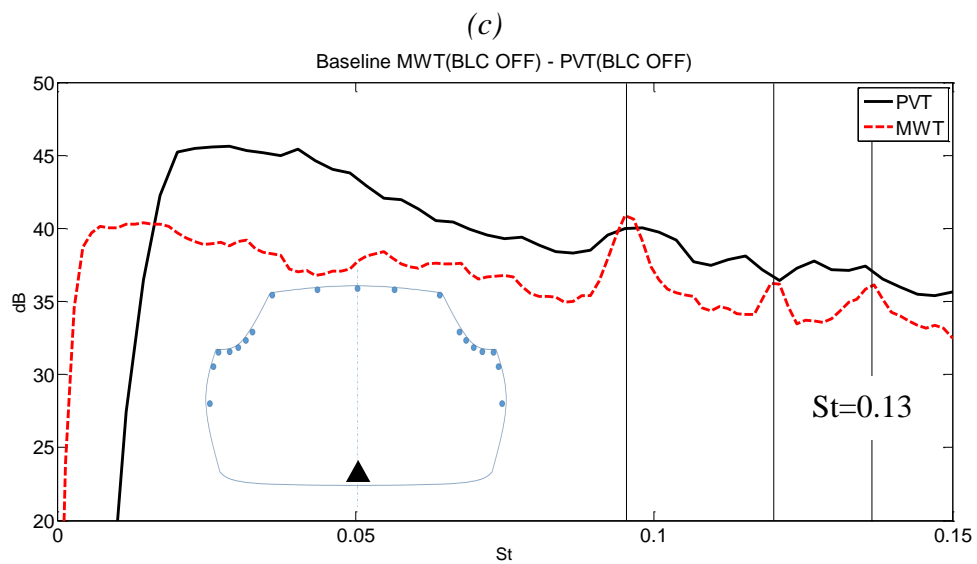
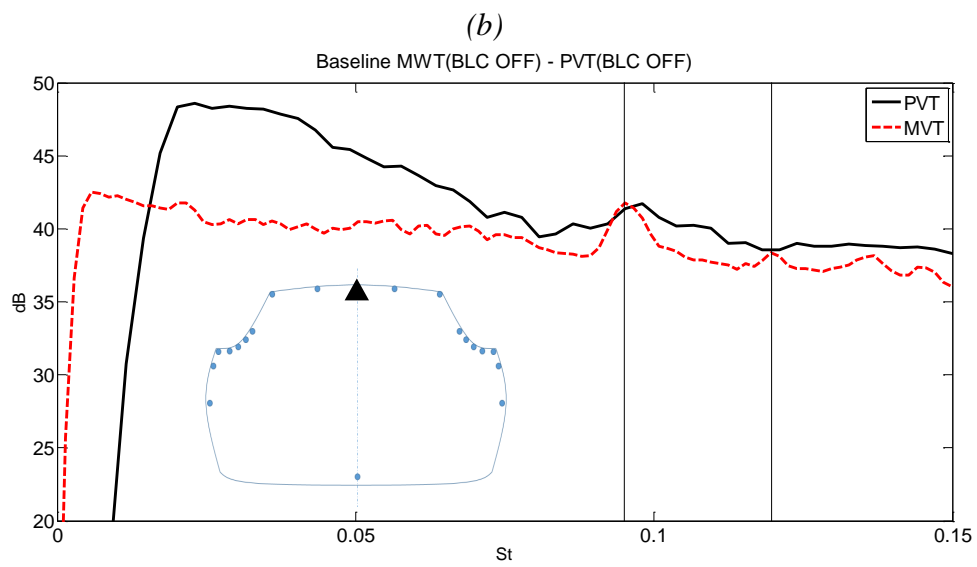
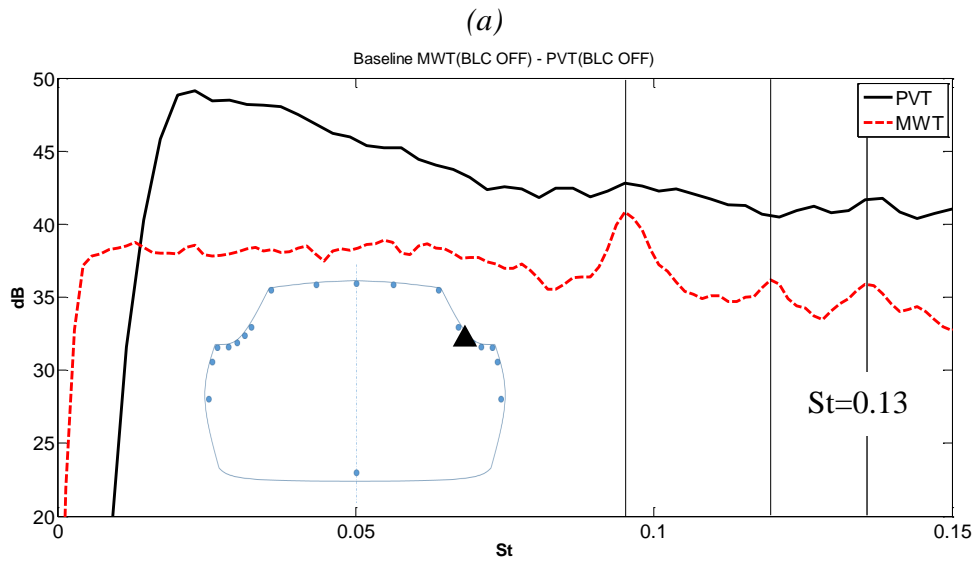
The wake center distributions in both lateral and vertical directions are found to be normal distributions, thus the pressure field in the near wake shows a stable behavior. The wake center distributions in the lateral direction cover a wider range than that in the vertical direction, which confirm the most dominating vortex shedding mode is in the lateral direction, namely the wake flapping. It is worth mentioning that Von Kármán vortex shedding modes are independent of the stability (stable or bi-stable) of the system [17]. The normal distribution discussed above does not deny the existences of the vortex shedding modes according to the POD analysis.

The most influential regions that alter the pressure field are found to be above the catwalk and on the catwalk, which provide insights on geometrical modifications for drag reduction. By limiting the range of the wake center distribution, the time-averaged wake size can be reduced.

5.3. Comparison of PVT and MWT Results

To minimize the background noise introduced by boundary layer control systems and the differences in tunnel-wall boundary layer developments, the results for the case of BLC off were compared. The PSDs for 6 sensors on the scaled model were calculated and compared with the full scale measurements at corresponding locations. The results for 4 sensors are reported in figure 5.13 a-d.





(d)

Figure 5.13: Pressure power spectral densities comparison between PVT and MWT: *a* sensor on the left side of catwalk, *b* sensor on the right side of catwalk, *c* sensor on the roof, *d* sensor on the rear bumper

Due to the scaling effect, flow phenomena in the near wake region are spread in a wider range in the frequency domain. Distinguished peaks in the power spectrums can be identified clearly from the model wind tunnel tests. The most recurrent peaks are found at $St= 0.096$ and $St=0.12$. Figure 5.13 b and d present energy peak at $St=0.13$. However, none of them are related to vortex shedding modes as discussed in the next section.

5.4. Coherence analysis

An effective method of relating the energy peaks observed in power spectrums to flow phenomena is to perform coherence and coherence phase analysis. A reference signal was acquired at the same time with the two different pressure transducer. By computing the point of maximum cross-correlation between the two reference acquisitions, The measurements can be resynchronized, allowing the calculation of the coherence function.

The coherence function is a normalized cross-correlation in the frequency domain which indicates the linear relationship of two signals at each frequency [18].

$$\gamma_{xy}^2(\omega) = \frac{|S_{xy}(\omega)|^2}{S_{xx}(\omega)S_{yy}(\omega)}$$

Where $S_{xy}(\omega)$ is the cross spectral density function and $S_{xx}(\omega), S_{yy}(\omega)$ are the power spectral density functions for two signals x and y.

- For $S_{xy}(\omega) = 1$, the signals are completely correlated
- For $S_{xy}(\omega) = 0$, the signals are not linearly related.

The value of is reduced if the signals have a non-linear relationship or if extraneous noise is present in the signals. The phase between the two signals is defined as the angle of the complex cross-spectrum function.

$$\varphi_{xy}(\omega) = \text{artan}\left(\frac{\text{Im}\left[\left(S_{xy}(\omega)\right)\right]}{\text{Re}\left[\left(S_{xy}(\omega)\right)\right]}\right)$$

- For $\varphi_{xy}(\omega) = 0^\circ$, the signals are in phase
- For $S_{xy}(\omega) = \pm 180^\circ$, the signals are out of phase.

The results for coherence of opposite positions are given in figure 5.14 a. for Left-to-right, and figure 5.14 b. for Top-to-bottom.

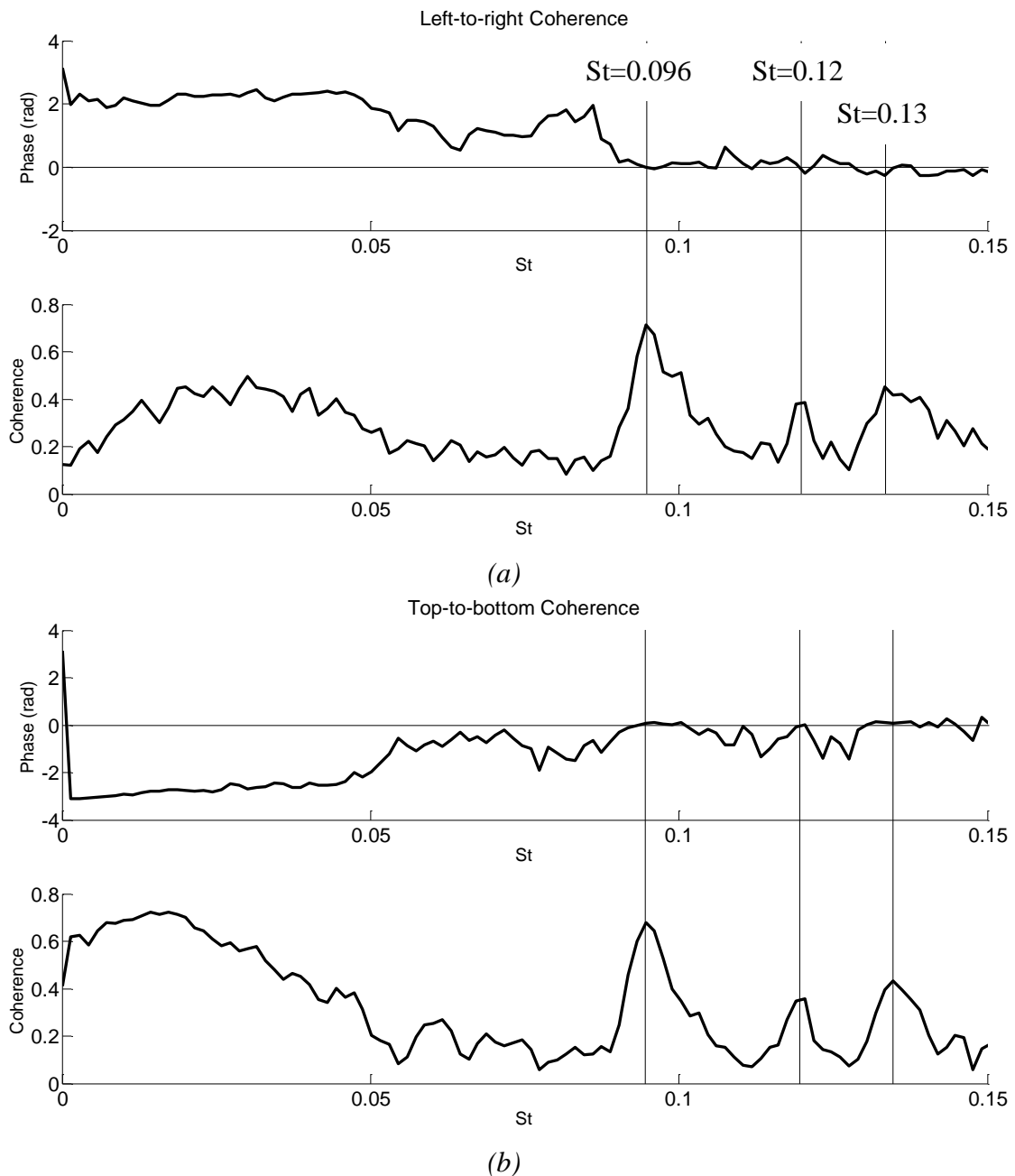


Figure 5.14: Coherence of opposite positions on the model base: **a** Left-to-right, **b** Top-to-bottom

It is found that the pressure fluctuations establish a strong coherence at $St=0.096$. The coherence functions of the measurements also present local peaks at $St=0.12$ and at $St=0.13$ with non-negligible levels of coherence (30% and 40% respectively).

As a rule, the Von Kármán mode is characterized by strong coherence signals with opposite phase angle. The pressure signals mentioned above are clearly in phase disregarding the directions in which the coherence functions were calculated, which confirm that these flow structures cannot be interpreted as Von Kármán modes.

6. Conclusion

The flow quality in the test section has been investigated. A numerical model for tunnel-wall boundary layer prediction was developed with high accuracy in boundary layer thickness estimation. The impacts of the boundary layer control system on the flow quality were identified and the local loss factor was found to be 0.01. The induced drag due to horizontal buoyancy was found to be 1.246N at airspeed of 50m/s.

The measurement quality has been studied by repeatability tests. The recommended test airspeed of 50m/s and yaw sweep range [$-10^\circ, 10^\circ$] were determined for highest repeatability accuracy. The confidence interval for aerodynamic force measurement was obtained.

Comparative force measurements between PVT and MWT have been performed. Due to differences in the Reynolds numbers and boundary layer control systems, accurate aerodynamic forces and moments cannot be obtained. However, the MWT established acceptable trend predictions regarding drag and frontal axle lift. Higher accuracy in lift prediction can be expected if the ground clearance between test floor and wheels is zero.

Unsteady base pressure measurements have been performed. Three near wake structures were identified for the full scale wind tunnel tests using POD analysis. The most dominating phenomenon was found to be the wake flapping effect, which was confirmed by wake center analysis. The spatial distributions for the wake center were determined in vertical and lateral directions, which provide insight on wake size control and drag reduction. Due to complex nature of the near wake and the presence of mechanical noise in the full scale wind tunnel, no evident energy peak was identified in the power spectrum.

The model wind tunnel was found to be fully efficient to capture the flow dynamics due to the scaling effect in the frequency domain. Three low-frequency activities in the near wake were identified at $St=0.096$, $St=0.12$, $St=0.13$. The physical origins of these universal phenomena are unknown and it requires further investigation to understand. It is also worth mentioning that due to the space limitation on the scaled model, careful preparation is required before any unsteady measurement.

References

1. B.R Munson, " *Fundamentals of Fluid Mechanics* ", Fig 9.24 Page 600.
2. Volvo Model Wind Tunnel User Manual
3. Cox D.R., Hinkley D.V. Chapman & Hall, " *Theoretical Statistics* ", 1974.
4. W.C. Steinle. " *The experimental determination of aerodynamic total pressure losses for heat exchanger surface considered for the 7*10 foot transonic wind tunnel* ", DTMB aero report, 1951.
5. Lachmann,G.V. " *Boundary layer control* ", Pergamon Press, 1961.
6. E.R.Spaulding. " *Comparative tests of Pitot-Static tubes* ", TN 546, 1935.
7. F.M. White. " *Fluid Mechanics* ", McGraw-Hill, 5th Edition, 2003.
8. J. Nikuradse. " *Laws of flow in rough pipes (Stromungsgesetze in Rauhen Rohren)*, VDI-Forschungsheft", vol. 361, 1933.
9. Naixing Chen John Wiley & Sons. " *Aerothermodynamics of Turbomachinery: Analysis and Design* ", 2011.
10. F.L.wattendorf. " *Factors influencing the energy ratio of return flow wind tunnels* ", 5th international congress for applied mechanics, Cambridge, 1938, p. 526.
11. A.Cogotti. " *Aerodynamic characteristics of car wheels, Impact of Aerodynamics on Vehicle Design* ", Int. J. of Vehicle Design, SP3, London ,1983, p. 173–196.
12. W. Hucho. " *Aerodynamics of Road Vehicles: Aerodynamics of Road Vehicles* ", Elsevier, 2013, p405.
13. David Sims-Williams, David Marwood and Adam Sprot, " *Links between Notchback Geometry, Aerodynamic Drag, Flow Asymmetry and Unsteady Wake* ", SAE International Journal of Passenger Cars-Mechanical Systems, Volume 4, Issue 1.
14. D. B. Sims-Williams and R. G. Dominy and J.P. Howell, " *An Investigation into Large Scale Unsteady Structures in the wake of real and idealised Hatchback Car Models* ",SAE Technical Papers, SAE 2001 World Congress Detroit, Michigan March 5-8 , 2001.
15. Berger E, Scholz D, Schumm M. " *Coherent vortex structures in the wake of a sphere and a circular disk at rest and under forced vibrations* ". J Fluids Struct 4(3):231–257, 1990.
16. Elliott Varon, Yoann Eulalie, Sèphie Edwige, Philippe Gilotte, Jean-Luc Aider," *The chaotic dynamics of a turbulent wake*", Cornell University Library.
17. Grandemange M. " *Analysis and control of three-dimensional turbulent wakes: from axisymmetric bodies to road vehicles* ". PhD thesis, ENSTA ParisTech, 2013
18. Hardin, J. C. " *Introduction to Time Series Analysis, NASA Reference Pub* ". 1145, 1990, pp. 39 - 47

Appendix

1. Total pressure loss due to BLC

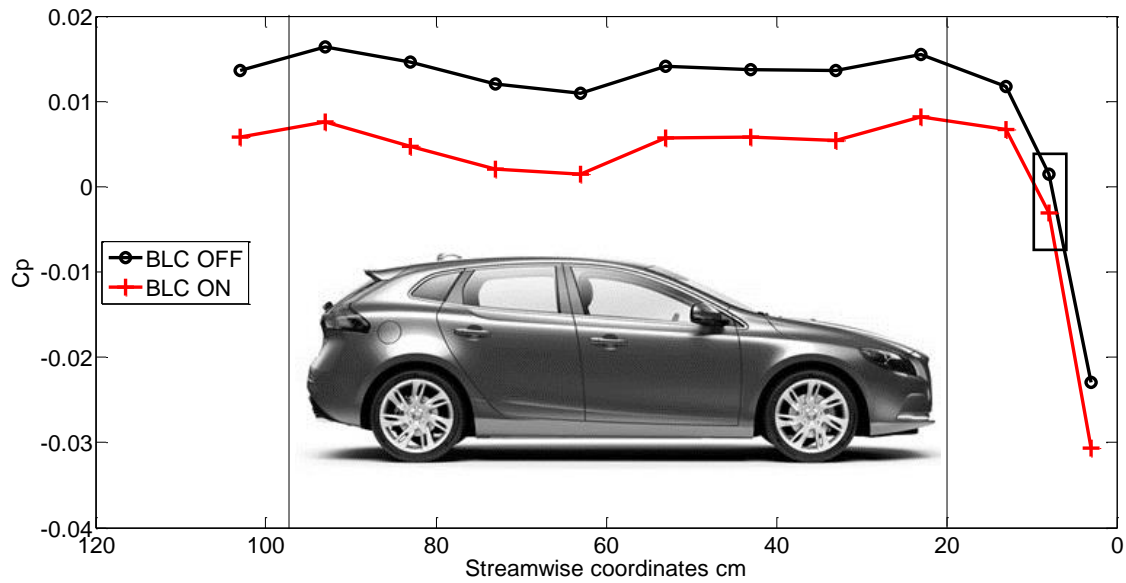


Fig A1: Static pressure distribution along the test section

The static pressure distributions drifted apart after the second measurement point (highlighted in black box), which could imply that new sources of pressure loss are introduced into the flow due to the boundary layer control system. Otherwise, the static pressure distribution curve for BLC on should be parallel to the curve of BLC off. It is known that flow recirculation through a sudden expansion could result in pressure loss, shown in figure below.

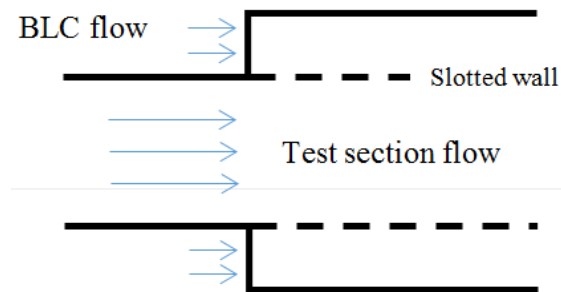


Fig A2: Flow recirculation through sudden expansion

The BLC flow tends to reduce the recirculation effect, but at the same time it introduces a shear layer between BLC flow and test-section flow due to large difference in the streamwise velocity. The instability of the shear layer is suspected to be the reason for total pressure loss. This is confirmed by total pressure measurement behind the suction area.

Experiment setup

The total pressure distribution behind the distributed suction area is measured using total pressure rake with equal space resolution of 10 mm in the vertical direction. The measurement area is shown in figure A3.

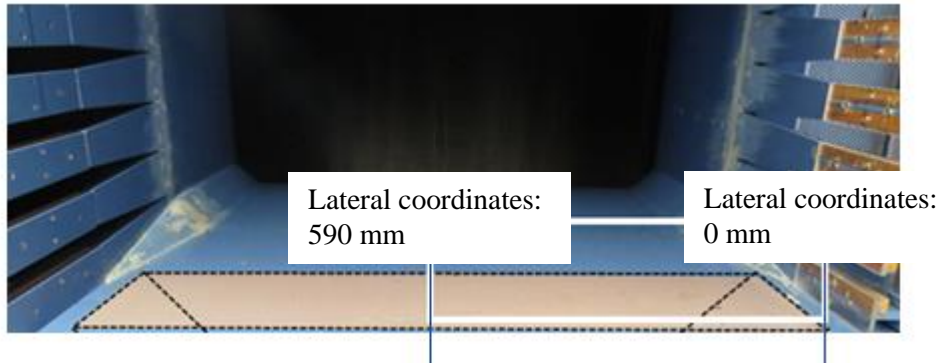
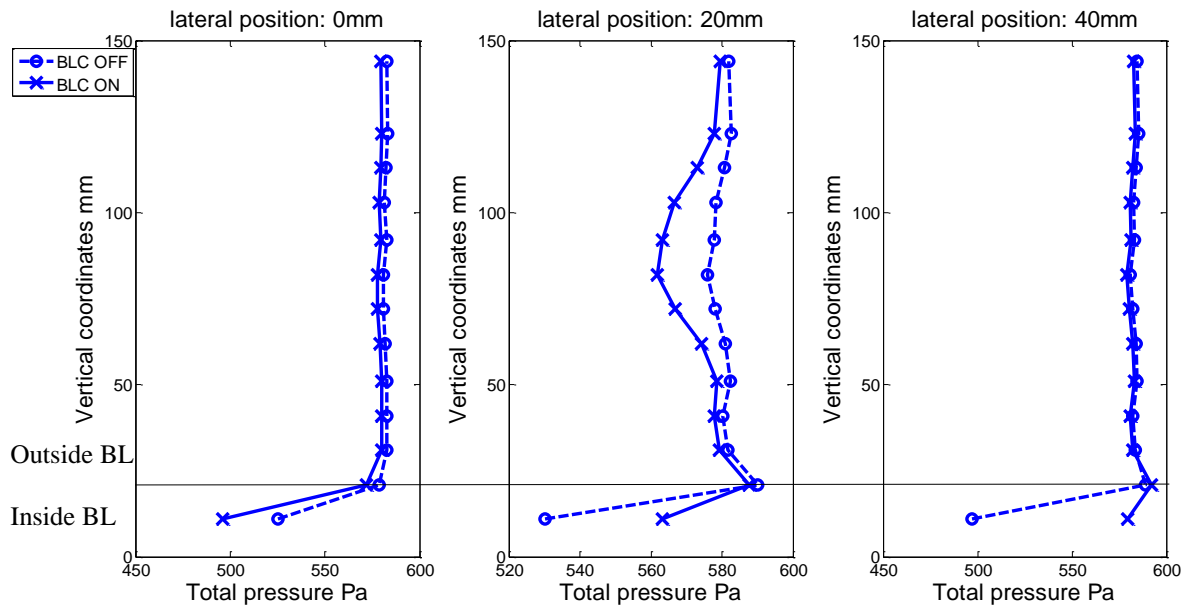


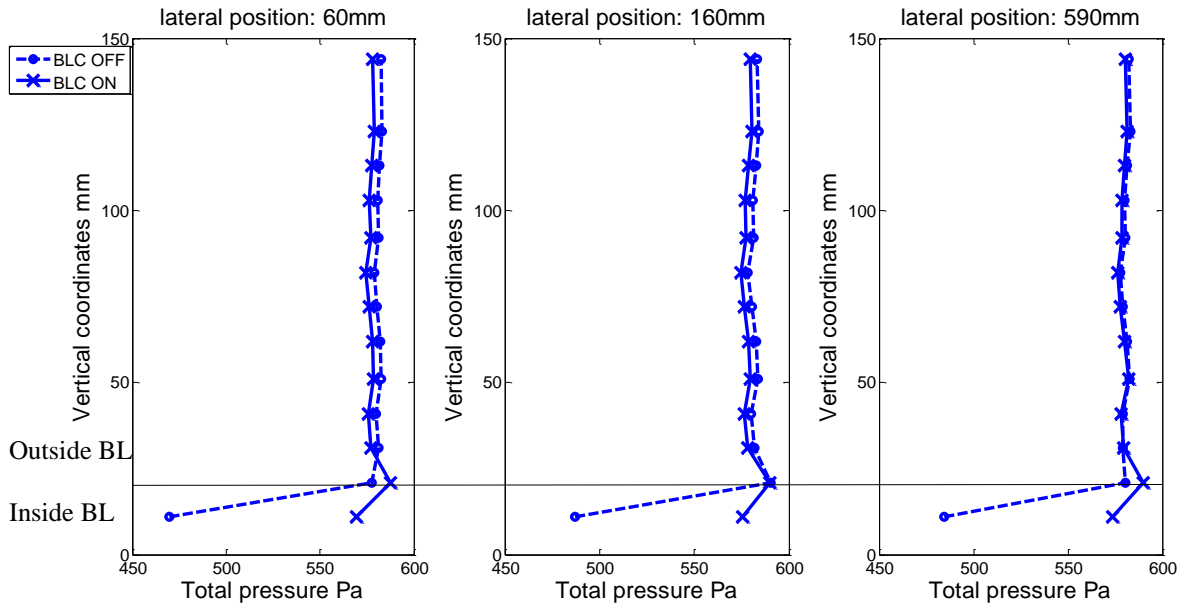
Fig A3: Measurement area

Results and discussion

Total pressure distributions at different lateral positions are given in figure A4 a. and b.



(a)



(b)
 Fig A4: Total pressure distribution behind the BLC system

It is known that vortices will emerge due to instabilities of the shear layer, which merge and form into large coherent structures. The characteristic scales are large enough to transport into the test section flow. The vortical structures are observed by large deviations in total pressure distribution are found at lateral position at 20 mm, which implies a large-scale structure (around 50 mm in vertical direction), is introduced to the test section flow when the BLC is operating. Furthermore, the unsteady coherent structures are also observed through the vibrations of the total pressure rake when it is placed near the slotted wall.

2. Moments repeatability

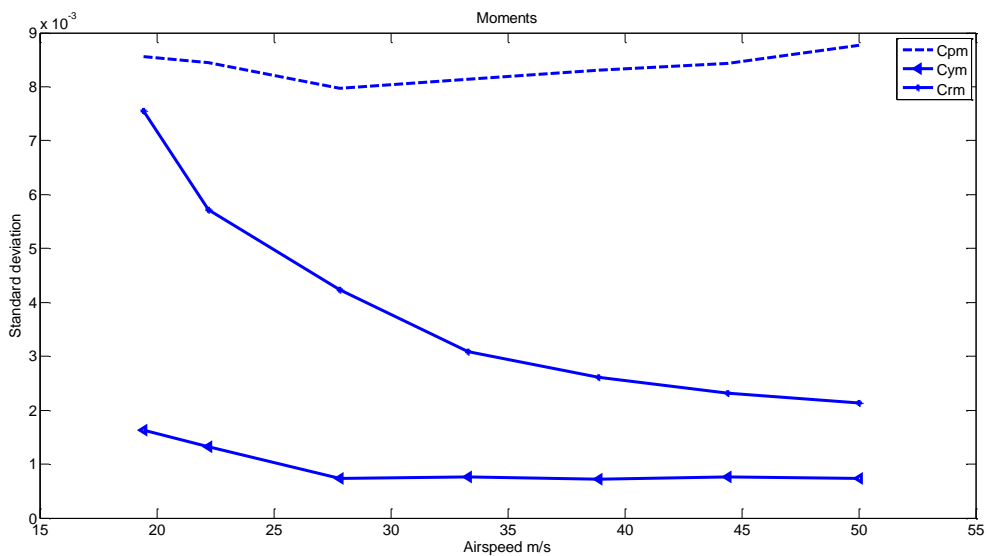


Fig A5: Airspeed dependence on moments' repeatability of square back

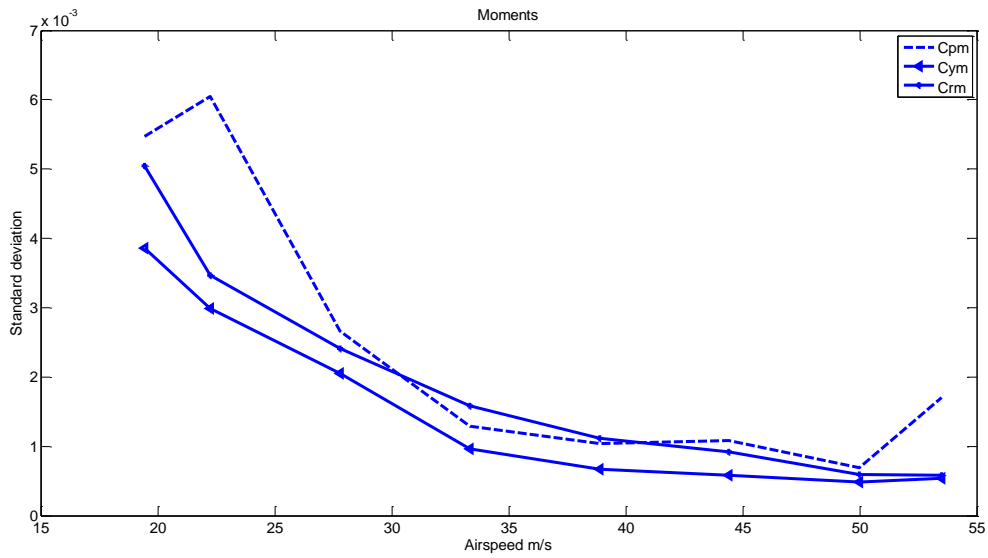


Fig A6: Airspeed dependence on moments' repeatability of fastback

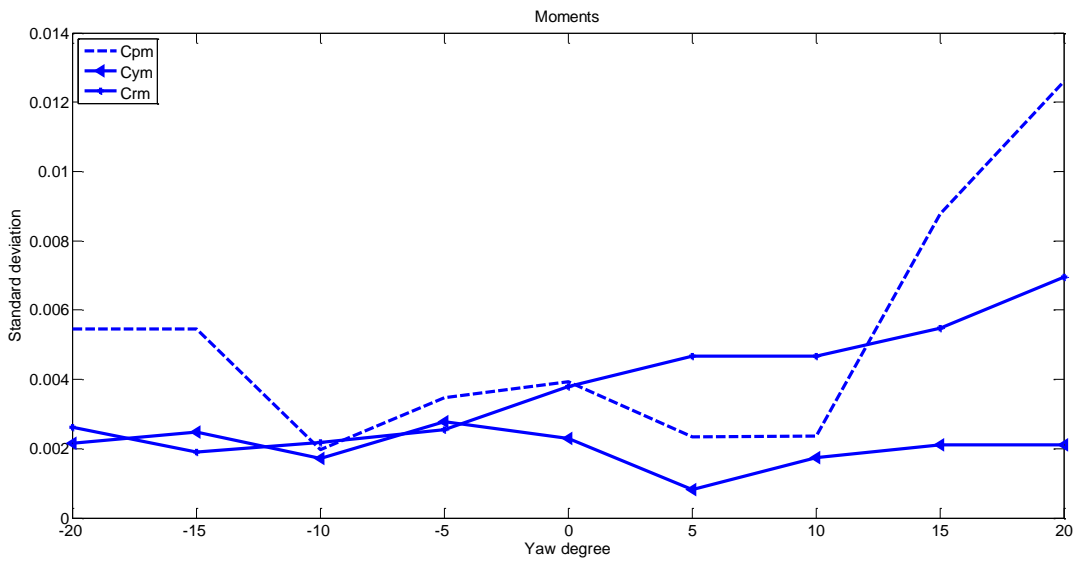


Fig A7: Yaw dependence on moments' repeatability of square back

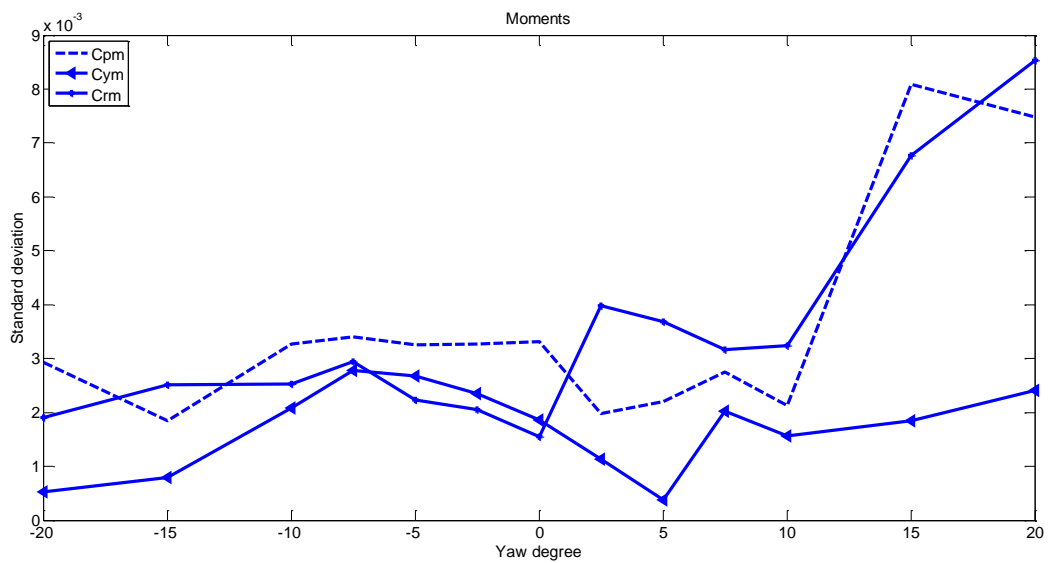


Fig A8: Yaw dependence on moments' repeatability of fastback

3. POD Mode 3

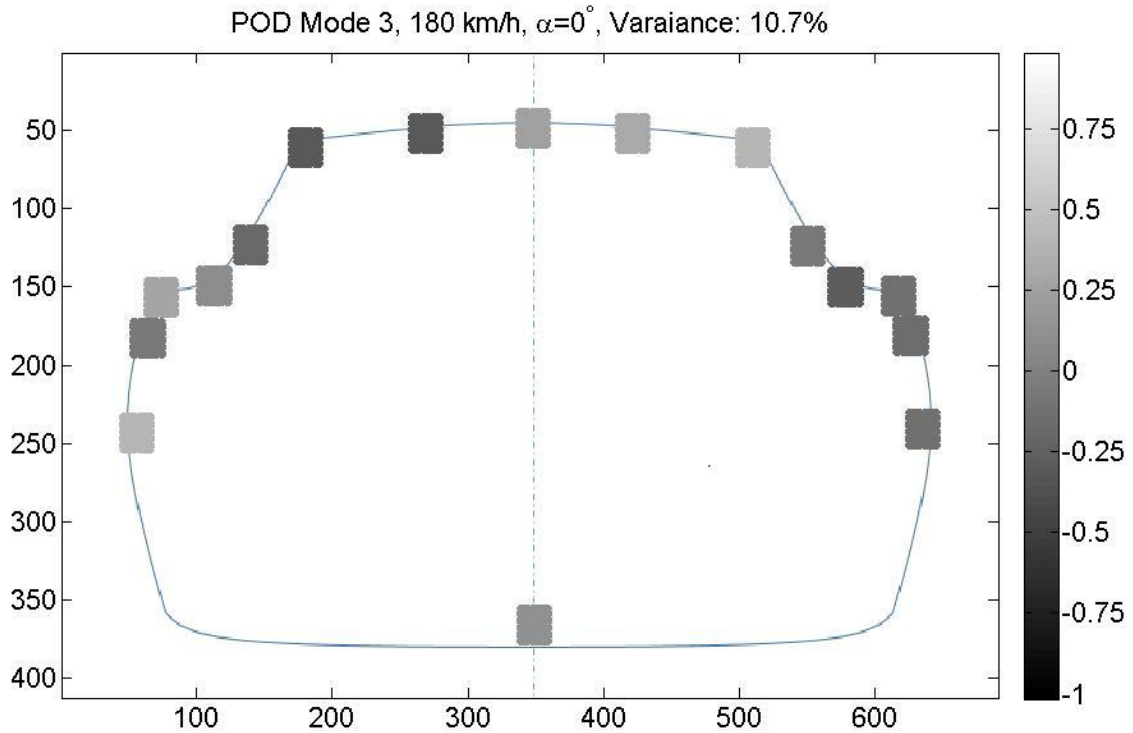


Figure A9: POD Mode 3

4. Different Configurations tested in Model Wind Tunnel

Configuration	ΔC_d	ΔC_{lf}	ΔC_{LR}	$\Delta C_d * A$
Baseline	REF.	REF.	REF.	REF.
Front chin spoiler	0.014	0.085	-0.058	0.002
Front Bumper	0.033	0.061	-0.084	0.003
Front bumper with splitter	-0.002	-0.010	-0.001	0.000
front wheel deflector	0.010	-0.035	0.034	0.001
front wheel deflector extended in x-direction	0.006	-0.002	0.019	0.001
side skirt 1	0.010	0.074	-0.003	0.001
side skirt with guide vanes	0.011	0.019	-0.018	0.001
front wheel deflector extended +side skirt with guidevanes	0.025	-0.060	-0.007	0.002
front chin +side skirt with guidevanes	0.011	0.171	0.048	0.001
taped front slot +side skirt with guidevanes+ front chin	0.018	0.154	0.039	0.002
taped front slot+ side skirt 2 inwards+ front chin	0.011	0.169	0.049	0.001
side skirt +front chin	0.013	0.175	0.059	0.001
side_skirt1_inwards	0.009	0.176	0.061	0.001
rear added diffuser only	0.005	0.021	-0.048	0.001
rear added diffuser extended	0.001	0.016	-0.048	0.000
rear added diffuser+ extended wheel deflector	0.015	0.016	-0.014	0.002
added rear diffuser extended+extended wheel deflector	0.016	0.015	-0.018	0.002
extended diffuser straight	0.011	0.052	-0.041	0.001
double extended diffuser	0.021	0.044	-0.115	0.002
front slot covered +front wheel half covered	-0.011	0.013	0.001	-0.001

front slot covered+ front wheel half covered+ extended diffuser	0.009	0.062	-0.009	0.001
front slot covered+all wheel half covered	-0.011	0.013	0.001	-0.001
front wheel slot covered	0.008	-0.021	-0.010	0.001
all wheels partially covered	-0.011	0.010	-0.033	-0.001
all wheels fully covered	-0.027	0.087	0.003	-0.002
all wheels partially covered less diverging	-0.029	0.043	-0.003	-0.002
front guide vane only	0.003	0.016	-0.003	0.001
front wheels partailly covered less diverging	-0.029	0.043	-0.003	-0.002
rear diffuser extended bend only	0.005	0.033	-0.020	0.001
rear diffuser extended bend front slot covered	0.017	0.011	-0.022	0.002
rear wheel fully covered	-0.026	0.037	0.006	-0.002
all wheelhouse covered	0.002	-0.006	0.000	0.000
all wheels partially covered summation sign type wheel deflector	-0.007	0.027	-0.021	0.000
summation sign type wheel deflectors only	0.009	0.050	-0.001	0.001
front wheelhouse covered only	0.003	-0.009	0.002	0.001
guide vane bent	0.009	-0.004	-0.005	0.001
guide vane shifted behind	0.022	-0.019	-0.015	0.002
guide vane shifted forward	0.011	-0.004	-0.012	0.001
spoiler conf 1	0.000	0.002	0.024	0.000
spoiler conf 2	0.010	0.004	-0.013	0.001
spoiler no sides	0.001	0.011	-0.004	0.000
wedges inside front wheel	-0.003	-0.003	-0.003	0.000
blades front wheelhouse	-0.001	-0.008	0.004	0.000
wedges inside all wheel	-0.003	-0.006	-0.003	0.000
windscreen spoiler	0.016	-0.002	0.009	0.002
plastic wedges inside front wheel house	-0.003	-0.001	0.003	0.000
metal wedges front wheel	-0.003	0.000	0.004	0.000
metal wedges front wheel one wedge rear wheel house	-0.001	-0.006	-0.004	0.000
step spoiler parallel to test floor	0.000	0.000	0.007	0.000
step spoiler pointing upwards	0.007	-0.009	-0.005	0.001
curved wedge front wheel	-0.003	0.004	-0.005	0.000
Scoop1	-0.004	-0.012	0.001	0.000
scoop rear wheels	-0.002	-0.002	0.029	0.000
diffuser angle 5.45	0.001	-0.001	-0.002	0.000
diffuser angle 4.588	0.002	0.000	0.010	0.000
diffuser angle 3.44	0.001	-0.001	0.006	0.000
diffuser angle 2.5	0.000	0.000	0.022	0.000
diffuser angle 2.005	0.004	-0.005	0.030	0.000
front wheel deflectors	0.004	-0.037	0.017	0.000
inside wheel cover diffuser angle 3.44	0.000	-0.006	0.001	0.000
inside wheel cover diffuser angle 2.5	0.001	-0.006	0.025	0.000
windscreen guidevanes	0.016	0.000	0.013	0.001
tail release wedges middle conf 1	0.002	-0.001	-0.011	0.000
tail release wedges middle conf 2	0.001	0.000	-0.002	0.000
tail release inwards towards the rear	0.001	0.001	-0.009	0.000
tail release edge tangential	0.000	0.000	-0.006	0.000

inner wheelhouse cover	0.000	0.025	-0.004	0.000
ride height increased by 1.5mm	0.004	0.000	-0.007	0.000
inner wheel house covered	-0.002	0.033	0.007	0.000
inner wheelhouse of all wheels covered	0.008	0.015	-0.008	0.001
inner wheelhouse covered front wheels	0.003	0.016	0.008	0.000
rear wheel slot covered	0.000	-0.002	0.002	0.000
inner wheelhouse covered with foam	0.003	0.016	0.006	0.000
front wheel house guide vanes	-0.002	-0.003	-0.001	0.000
front wheel house guide vanes forward	-0.006	0.006	-0.002	0.000
front wheel house guide vane overall	-0.004	0.003	0.000	0.000
guide vane on all the wheel houses	-0.004	0.005	0.002	0.000
a-pillar scania	0.010	-0.006	-0.005	0.001
a_pillar scania flipped	0.015	-0.002	-0.011	0.001
front wheel rim covered completely	-0.002	0.000	-0.001	0.000
Front wheel cover without covering the front slot	-0.001	-0.031	-0.003	0.000
bl scoop sfor all wheels	0.005	-0.050	-0.022	0.000